Timing of closure of the Meso-Tethys Ocean: Constraints from remnants of a 141–135 Ma ocean island within the Bangong–Nujiang Suture Zone, Tibetan Plateau

Jian-Jun Fan[1, 2*], Yaoling Niu[2], Yi-Ming Liu[3], Yu-Jie Hao[4]

[1]*College of Earth Sciences, Jilin University, Changchun, 130061, P.R. China*

[2]*Department of Earth Sciences, Durham University, Durham DH1 3LE, UK*

[3]*Key Lab of Submarine Geosciences and Prospecting Techniques, Ministry of Education, and College of Marine Geosciences, Ocean University of China, Qingdao 266100, Shandong, China*

[4]*Key Laboratory of Mineral Resources Evaluation in Northeast Asia, Ministry of Natural Resources of China, Changchun, 130061, P.R. China*

***Corresponding authors:** E-mail addresses: fanjj03@163.com **(J.-J. Fan)**

ABSTRACT

A knowledge of the timing of closure of the Meso-Tethys Ocean represented by the Bangong–Nujiang Suture Zone (BNSZ), i.e., the timing of the Lhasa-Qiangtang collision, is critical for understanding the Mesozoic tectonics of the Tibetan Plateau. But this timing is hotly debated with existing suggestions varying from Middle Jurassic (ca. 166 Ma) to Late Cretaceous (ca. 100 Ma). In this study, we describe the petrology of the Zhonggang igneous–sedimentary rocks in the middle segment of the BNSZ, and present results of zircon U–Pb geochronology, whole-rock geochemistry, and Sr–Nd isotope analysis of the Zhonggang igneous rocks. The Zhonggang igneous–sedimentary rocks have a thick basaltic basement (> 2 km thick) covered by limestone with interbedded basalt and tuff, trachyandesite, chert, and poorly-sorted conglomerate comprising limestone and basalt debris. There is an absence of terrigenous detritus (e.g., quartz) within the sedimentary and pyroclastic rocks. These observations, together with the typical exotic blocks-in-matrix structure between the Zhonggang igneous–sedimentary rocks and the surrounding flysch deposits, lead to the conclusion that the Zhonggang igneous–sedimentary rocks are remnants of an ocean island within the Meso-Tethys Ocean. This conclusion is consistent with the ocean island basalt-type geochemistry of the Zhonggang basalts and trachyandesites, which are enriched in light rare earth elements ($(La/Yb)_N$ = 4.72–18.1 and 5.61–13.7, respectively) and have positive Nb–Ta anomalies (Nb_{PM}/Th_{PM} > 1, Ta_{PM}/U_{PM} > 1), low initial $^{87}Sr/^{86}Sr$ ratios (0.703992–

0.705428), and positive mantle $\varepsilon_{Nd}(t)$ values (3.88–5.99). Zircon U–Pb dates indicate that the Zhonggang ocean island formed at 141–135 Ma; therefore, closure of the Meso-Tethys Ocean and collision between the Lhasa and Qiangtang terranes must have happened after ca. 135 Ma.

INTRODUCTION

The Tibetan Plateau is the highest topographic feature on Earth. It consists of Gondwana-derived terranes that accreted progressively onto the southern margin of Eurasia during the Phanerozoic opening, growth, and closure of the Paleo-, Meso- and Neo-Tethys oceans (Fig. 1a; Yin and Harrison, 2000; Zhu et al., 2013; Metcalfe, 2013; Xu et al., 2015; Kapp and DeCelles, 2019).

The Meso-Tethys Ocean, which is represented by the Bangong–Nujiang Suture Zone (BNSZ) in the central Tibetan Plateau, places important constraints on the Mesozoic tectonic history of the Tibetan Plateau (Kapp et al., 2007; Pan et al., 2012; Zhang et al., 2014a; Zhu et al., 2016), and provides insights into widespread late Mesozoic mineralization within central Tibet (Geng et al., 2016; Li et al., 2018). The BNSZ has been studied extensively since the 1980s (Allègre et al., 1984; Yin and Harrison., 2000; Kapp et al., 2007; Pan et al., 2012; Shi et al., 2008, 2012; Zhang et al., 2014a, 2017; Li et al., 2014, 2018, 2019 a, b, 2020; Zhu et al., 2016; Wang et al., 2016; Zeng et al., 2016; Geng et al., 2016; Liu et al., 2017; Chen et al., 2017; Fan et al., 2019a; Hao et al., 2019; Yan and Zhang, 2020; Tang et al., 2020), but many aspects about the evolution of the Meso-Tethys Ocean remain controversial. The timing of closure of the Meso-Tethys Ocean is central to these controversies.

Timing of closure of the Meso-Tethys Ocean are commonly assigned to the latest Jurassic (ca. 145 Ma) because ophiolitic rocks and flysch deposits in the BNSZ overlain by Upper Jurassic to Lower Cretaceous shallow-marine strata, and the 140–130 Ma arc-related pause in igneous activity within the southern Qiangtang Terrane were interpreted to result from the Lhasa-Qiangtang collision (Girardeau et al., 1984; Wang and Dong, 1984; Chen et al., 2004; Zhu et al. 2016; Huang et al., 2017; Li et al., 2019a, b). Some studies suggest that the Meso-Tethys Ocean closed as early as Middle Jurassic (ca. 166 Ma), based on a Middle Jurassic unconformity and associated shift in provenance from arc-related to uplifted orogenic source within the southern Qiangtang Terrane, consistent with a major tectonic event such as the Lhasa–Qiangtang collision (Ma et al., 2017).

These ideas of early (ca. 166 or ca. 145 Ma) Meso-Tethys Ocean closure, however, cannot explain the well-exposed Early Cretaceous igneous rocks (e.g., basalt, trachyandesite and gabbro) and the related sedimentary rocks (e.g., limestone and chert) in the Zhonggang and Tarenben areas of the BNSZ (Figs. 1b–1c). The geochemistry of the Early Cretaceous basalts resembles those of modern ocean island basalts (OIB); therefore, some studies inferred that they record intraplate ocean island magmatism (Zhu et al., 2006; Bao et al., 2007; Fan et al., 2014, 2018a; Zhang et al., 2014a). In this case, the Meso-Tethys Ocean must have remained open until the Early Cretaceous (Fan et al., 2018a). Therefore, the interpretation of early closure times (ca. 166 or ca. 145 Ma) needs revision. The abundant late Mesozoic mineralization in central Tibet must be genetically associated with the Meso-Tethys seafloor subduction (Li et al., 2014; Fan et al., 2015).

However, the question is whether the Early Cretaceous geochemically OIB-like igneous rocks and the related sedimentary rocks in the Zhonggang and Taronben areas of the BNSZ indeed represent remnants of intraplate ocean islands. Some studies suggest these rocks formed in a marine setting on continental crust after the Lhasa–Qiangtang collision, rather than as ocean islands in deep water (Zhu et al., 2016; Huang et al., 2017; Li et al., 2019a, b). In this model, the source of the igneous rocks was enriched asthenosphere that ascended through slab windows formed by slab break-off after the Lhasa–Qiangtang collision (Zhu et al., 2016; Wu et al., 2018), and the sedimentary rocks formed within a post-collisional submarine basin (Zhu et al., 2016; Li et al., 2019a).

In this study, we present detailed petrological descriptions of the igneous and sedimentary rocks in the Zhonggang area, and results of U–Pb zircon geochronology, whole-rock geochemistry, and Sr-Nd isotope analysis of the igneous rocks. All these data show a strong affinity of the Zhonggang igneous–sedimentary rocks association with an intraplate ocean island, allowing us to conclude that they were remnants of an ocean island in the Meso-Tethys Ocean. The new U–Pb ages of the Zhonggang igneous rocks are Early Cretaceous (141–135 Ma), consistent with late closure of the Meso-Tethys Ocean and Lhasa–Qiangtang continental collision after ca. 135 Ma.

GEOLOGICAL BACKGROUND

The Tibetan Plateau is located within the eastern Alpine–Himalayan tectonic domain, and is divided into the Himalayan, Lhasa, southern Qiangtang, northern Qiangtang, Bayan Har–Garze, and Qaidam terranes. These terranes are separated by the Indus–Yarlung Zangbo (IYZSZ), Bangong–Nujiang (BNSZ), Longmuco–Shuanghu–Lancangjiang (LSLSZ), Jinshajiang (JSSZ), and East Kunlun–A'nyemaqen (EKASZ) suture zones, respectively (Fig. 1a; Allégre et al. 1984; Yin and Harrison. 2000; Pan et al. 2012; Metcalfe, 2013; Zhu et al., 2013; Zhai et al., 2016). It is generally accepted the three suture zones (EKASZ, JSSZ, and LSLSZ) in northern Tibet represent remnants of the Paleo-Tethys that opened in the early Paleozoic and closed in the Permian–Triassic, whereas the IYZSZ in southern Tibet represents the Neo-Tethys mainly developed in the Mesozoic (Fig. 1a; Yin and Harrison, 2000; Pan et al., 2012; Metcalfe, 2013; Zhu et al., 2013; Xu et al., 2015; Zhai et al., 2013, 2016; Hu et al., 2014, 2015; Kapp and DeCelles, 2019).

The BNSZ in central Tibet forms the boundary between the Lhasa and southern Qiangtang terranes (Fig. 1a), and represents the remnant of the Meso-Tethys (Girardeau et al., 1984; Metcalfe, 2013; Zhai et al., 2013; Zhang et al., 2014a; Chen et al., 2017; Fan et al., 2017; Kapp and Decelles, 2019). This suture zone extends eastward for ~2500 km from Kashmir to the Bangong Co, Gerze, Dongqiao, Amdo, Dengqen, and Jiayuqiao areas (Allégre et al., 1984; Girardeau et al., 1984; Pan et al., 2012). At its eastern end, this suture zone connects with the Myitkyina, Meratus, and Lok-Ulo suture zones of Southeast Asia (Metcalfe, 2013; Liu et al., 2016).

The BNSZ is dominated by scattered fragments of latest Paleozoic to Mesozoic ophiolites (Shi et al., 2012; Wang et al., 2016; Zhang et al., 2016, 2017; Wei et al., 2019), ocean island suites (Fan et al., 2014, 2017, 2018b; Zhang et al., 2014a), intra-oceanic arcs (Shi et al., 2008; Liu et al., 2014; Zeng et al., 2016; Huang et al., 2017; Tang et al., 2019; Fan et al., 2019; Yan and Zhang, 2020), flysch deposits (Huang et al., 2017; Fan et al., 2018a), and high-pressure metamorphic rocks (e.g., the Dongco eclogite; Zhang et al., 2016, 2017). In addition, widespread Paleozoic to Mesozoic sedimentary and volcanic rocks occur on both sides of the BNSZ (Zhang et al., 2013; Li et al., 2014, 2018, 2020; Chen et al., 2014; Fan et al., 2015; Liu et al., 2017; Hu et al., 2017). World-class porphyry copper–gold mineral deposits, formed at 170–110 Ma (e.g., Duolong deposit), and Fe, Pb–Zn, and W mineral deposits are documented in and around the BNSZ (Geng et al., 2016; Li et al., 2018).

PETROLOGY OF THE ZHONGGANG IGNEOUS–SEDIMENTARY ROCKS

Igneous and sedimentary rocks occur over an area of more than 400 km^2 within the Zhonggang area of the middle segment of the BNSZ (Fig. 2a; Fan et al., 2014). The Zhonggang igneous–sedimentary rocks are taupe, gray–green, and bright white in remote sensing images, and can be distinguished easily from the ophiolites and flysch deposits in the BNSZ (brown and gray–green) and Jurassic sedimentary strata on the southern Qiangtang Terrane (yellow–brown; Fig. 2b).

The Zhonggang igneous–sedimentary rocks comprise a thick basaltic basement (>2 km thick; Fig. 2c) beneath a cover sequence of limestone (Fig. 2c), limestone with intercalated basalt (Figs. 2d, 3a), basalt–tuff–limestone (Fig. 3b), interbedded limestone–tuff (Fig. 3c), basalt–trachyandesite–limestone (Fig. 3d), and trachyandesite–limestone (Fig. 3e). Despite slight modification by alteration (Fig. 4a), primary igneous textures of the basalt intercalated with the limestone are mostly preserved; it has spilitic textures, and contains skeletal microcrystalline plagioclase (Fig. 4a). The trachyandesite is in the upper part of the Zhonggang igneous–sedimentary rocks, and is conformable with the basalt and limestone (Figs. 3d–3e); it has interwoven textures, and contains weakly oriented microcrystalline plagioclase (Fig. 4b). The limestone in the cover sequence is compositionally pure with recrystallized calcite (Fig. 4c), and the tuff contains clasts and matrix, both of which are dominated by basalt and limestone (Fig. 4d).

Chert (Fig. 3f) and colluvial conglomerate (Fig. 3g) occur within the northeastern margin of the Zhonggang igneous–sedimentary rocks in the Zhagangnisang area (Fig. 2a). The chert contains minor calcite clasts in addition to chalcedony (Fig. 4e). The colluvial conglomerate contains gravels and matrix, both of which are entirely poorly sorted limestone (e.g., reef limestone) and basalt with angular to subangular shape (Figs. 3g, 4f), indicating a rapid accumulation of sediments with proximal and restricted provenance. Terrigenous detritus (e.g., quartz) was not observed within the limestone, chert, colluvial conglomerate, or tuff, indicating a setting distal to land. In the Zhanong area, the Zhonggang igneous–sedimentary rocks contain gabbro that intrudes as dykes into the basalt and limestone (Fan et al., 2014). In the Zhonggang area, the Zhonggang igneous–sedimentary rocks were thrust onto the Mugagangri Group, and formed widespread exotic blocks within the matrix of the flysch deposits (Figs. 3h–3i).

ANALYTICAL METHODS AND RESULTS

Methods for zircon U–Pb, whole-rock major- and trace-element, and Sr–Nd isotope analyses are provided in the Data Repository.

Whole-rock major- and trace-element geochemistry

A total of 38 samples (4 trachyandesite, 34 basalt, loss-on-ignition < 4 wt.%) were collected for whole-rock major- and trace-element analysis, some of which (2 trachyandesite, 32 basalt) are previous reported (Fan et al., 2014; Yu et al., 2015; Wang et al., 2016). Data are provided in Table DR1. The samples have undergone varying degrees of alteration (Fig. 4a), resulting in variable values of LOI and changes in the concentrations of mobile elements (e.g., Na, K, Ca, Cs, Rb, Ba, and Sr) compared with protolith values. However, concentrations and ratios of immobile elements (e.g., REE, Nb, Ta, Zr, Hf, Ti, and P) and transition metal elements (e.g., V, Ni, and Cr) have not been affected by these processes and can therefore be used to investigate the petrogenesis and tectonic setting of the samples (Verma, 1981; Hart and Staudigel, 1982; Hu et al., 2019).

The Zhonggang basalt samples have variable SiO_2 (44.9–52.5 wt.%) and MgO (3.29–8.56 wt.%) contents, variable $Mg^{\#}$ values [100 × molar Mg/(Mg + Fe)] (43–66), and high TiO_2 contents (1.90–4.57 wt.%). The Zhonggang trachyandesite samples have high SiO_2 (53.2–55.4 wt.%) and TiO_2 (1.78–2.21 wt.%) contents, and low MgO contents (1.58–2.46 wt.%) and Mg# values (26–41). All of the basalt samples are classified as alkaline basalts, based on the Nb/Y vs. Zr/TiO_2 classification diagram, and the trachyandesite samples are classified as trachyandesite and trachyte (Fig. 5; Winchester and Flody, 1977).

All of the Zhonggang trachyandesite and basalt samples are enriched in light rare earth elements (LREE; La_N/Yb_N = 5.61–13.7 and 4.72–18.1, respectively) and high-field-strength elements (Nb, Ta, Zr, and Hf), yielding chondrite-normalized REE patterns and primitive-mantle-normalized trace element patterns that are similar to those of OIB (Figs. 6a–6d; Sun and McDonough, 1989).

Zircon U–Pb ages

Three trachyandesite samples were selected for zircon U–Pb dating by laser ablation–inductively coupled plasma–mass spectrometry (LA–ICP–MS). Data are provided in Table DR2.

Zircon grains selected for dating included whole crystals and fragments of long euhedral crystals with lengths of 40–120 μm and length-to-width ratios of 1.5:1 to 3:1. All crystals are relatively homogeneous, and show oscillatory zoning in cathodoluminescence (CL) images (Fig. 7), consistent with an igneous origin (Belousova et al., 2002; Hoskin and Schaltegger, 2003). These zircons yield weighted mean $^{206}Pb/^{238}U$ ages of 141.0 ± 2.4 Ma (MSWD = 1.7), 140.0 ± 2.2 Ma (MSWD = 2.2), and 135.3 ± 2.5 Ma (MSWD = 0.9), respectively (Fig. 7).

Whole-rock Sr–Nd isotopic compositions

A total of 16 samples (2 trachyandesite samples, 14 basalt samples) were selected for whole-rock Sr–Nd isotope analysis in this and previous studies (Table DR3; Wang et al., 2016). Initial Sr isotope ratios and $\varepsilon_{Nd}(t)$ values were calculated using the new mean-age of ca. 140 Ma reported in this study.

The Zhonggang igneous rocks have a wide range of initial $^{87}Sr/^{86}Sr$ ratios (0.703992–0.705428), and positive $\varepsilon_{Nd}(t)$ values of +3.88 to +5.99 (Fig. 8). Strontium is more mobile than Nd during seawater alteration (Verma, 1981), so the wide range of initial $^{87}Sr/^{86}Sr$ ratios might reflect alteration.

DISCUSSION

Ages of the Zhonggang igneous–sedimentary rocks

The Early Cretaceous ages (e.g., whole-rock $^{40}Ar/^{39}Ar$ ages of 141–123 Ma of basalt, and zircon U-Pb ages of 132–116Ma of gabbro; Fig. DR1; Bao et al., 2007; Fan et al., 2014; Zhang et al., 2014a) from the Zhonggang igneous rocks indicate the formation timing of these rocks in the Early Cretaceous. However, some researchers suggest that these ages might be problematic, because the CL images of dated zircons from the gabbro are not typical of mafic rocks, and the Ar-Ar isotopic system of the basalts they have been reset (Ma et al., 2017; Li et al., 2019a). Therefore, the timing of formation of the Zhonggang igneous–sedimentary rocks remains controversial.

The dated trachyandesite is conformable with the basalt and limestone (Figs. 3d–3e), indicating that the age of the trachyandesite records the timing of formation of the Zhonggang igneous–sedimentary rocks. The zircon grains have broad, weakly-, or unzoned cores, and weak to strong zoning toward the rims (Fig. 7), typical of zircon grains within trachyandesites (Akal et al., 2012; Tang et al., 2012; Feng et al., 2015; Shu et al., 2017; Xu et al., 2019; Liu et al., 2020) and andesites (Wang et al., 2015; Zeng et al., 2016; Liu et al., 2018). Therefore, the zircon U–Pb ages of 141–135 Ma record the timing of crystallization of the trachyandesite. The new age data provide strong evidence for Early Cretaceous (141–135 Ma) formation of the Zhonggang igneous–sedimentary rocks.

Petrogenesis of the Zhonggang igneous rocks

The role of crustal contamination

Thorium and tantalum are sensitive indicators of crustal contamination, which increases Th/Ta ratios (Condie, 1993). All of the Zhonggang basalts and trachyandesites have relatively low Th/Ta ratios (0.57–2.76, and 0.47–1.16, respectively), similar to those of volcanic rocks derived from primitive mantle (Th/Ta = 2.3), and much lower than those of the upper crust (Th/Ta >10; Condie, 1993). This indicates that the basalts and trachyandesites were not contaminated by crustal material. Moreover, there is no negative correlation between SiO_2 and $\varepsilon_{Nd}(t)$ values (Fig. 9a), which is further evidence against crustal contamination.

Magma source

The REE characteristics of mafic rocks constrain the features of the magma source (McKenzie and O'Nions, 1991; Ellam, 1992; Zhao and Zhou, 2007). Basaltic magmas are commonly derived from the partial melting of mantle lherzolite, and their REE patterns are controlled mainly by the contents of garnet and spinel in their magma source rather than by the contents of olivine, clinopyroxene, or orthopyroxene, or by pressure and temperature (McKenzie and O'Nions, 1991; Horn et al., 1994; Schwandt et al., 1998; Oyan et al., 2017). In general, basalts derived from spinel lherzolite have flat chondrite-normalized REE patterns with weak or absent fractionation between LREE and heavy REE (HREE). However, HREE (e.g., Yb) are more compatible in garnet than the other REE (McKenzie and O'Nions, 1991; Oyan et al., 2017), so basalt derived from garnet lherzolite shows strong fractionation between LREE and HREE, and has high La_N/Yb_N and Ce_N/Yb_N ratios (McKenzie and O'Nions, 1991; Hart and Dunn, 1993; Hauri et al., 1994). In addition, partial melting of spinel lherzolite does not affect its Sm/Yb ratio, because Sm and Yb have similar partition coefficients; however, such melting might decrease the La/Sm ratio and Sm content of the melt (Aldanmaz et al., 2000). Therefore, partial melts of spinel lherzolite plot on melting trends sub-parallel to, and nearly coincident with, a mantle array defined by depleted to enriched source compositions (Fig. 9b; Aldanmaz et al., 2000). In contrast, garnet partitions Yb ($D_{garnet/melt}$ = 6.6) strongly relative to Sm ($D_{garnet/melt}$ = 0.25; Johnson, 1994), so partial melts of garnet lherzolite mantle with residual garnet define trends on plots of Sm/Yb vs. La/Sm that slope steeply relative to the trends defined by melts of spinel lherzolite (Fig. 9b; Aldanmaz et al., 2000; Zhao and Zhou, 2007).

The Zhonggang basalts have LREE-enriched chondrite-normalized REE patterns (La_N/Yb_N = 4.72–18.1, Fig. 6a), and high Ce_N/Yb_N ratios (4.52–14.7), similar to those of basalts derived from garnet lherzolite (McKenzie and O'Nions, 1991; Hart and Dunn, 1993; Hauri et al., 1994). Furthermore, the Zhonggang basalts plot in the field of garnet lherzolite on the Sm/Yb vs. La/Sm diagram (Fig. 9b; Aldanmaz et al., 2000). These observations indicate that the Zhonggang basalts formed by partial melting of a garnet lherzolite mantle source.

The Zhonggang trachyandesites have similar initial $^{87}Sr/^{86}Sr$ ratios and $\varepsilon_{Nd}(t)$ values to the Zhonggang basalts (Fig. 8). They have high Sm/Yb (3.22–4.45), and La/Sm (2.43–4.41) ratios, and they plot in similar positions to the basalts, within the field of garnet lherzolite on the Sm/Yb vs. La/Sm diagram (Fig. 9b). Moreover, the Zhonggang trachyandesites and basalts show a continuous evolutionary trend on the immobile elements (e.g., Si, Al, Nb, Ta, Th, and Ce) vs. MgO diagrams (Fig. DR2). These features lead to the conclusion that the Zhonggang trachyandesites were formed by fractional crystallization of the Zhonggang basalts.

Geodynamic setting of the Zhonggang igneous–sedimentary rocks

There are two possible geodynamic settings for the Zhonggang igneous–sedimentary rocks: (1) an ocean island sequence within a deep marine basin (Fan et al., 2014, 2018a); (2) an ocean island-like sequence formed in a collisional setting (Zhu et al., 2016; Li et al., 2019a). These settings are discussed below.

Ocean island sequences in deep ocean basins

The general view of ocean island sequence is mostly based on the prototypical Hawaiian model that formed on the fast moving Pacific plate (Ramalho et al., 2010a). The Hawaiian ocean islands record an initial basement-building stage, with frequent and voluminous eruptions of OIB-type lava. Towards the end of basement-building, the plate moves away from the hotspot center and magmatism diminished gradually. Erosion, mass-wasting events, and cooling and sinking of plates cause ocean islands to subside and eventually disappear beneath the surface of the ocean as submarine guyots and seamounts (Darwin, 1842; Menard and Ladd, 1963; Detrick and Crough, 1978; Grigg, 1982; Menard, 1983; Morgan et al., 1995; Ramalho et al., 2010a). Limestone cover sequence deposited on the guyot is expected to receive little magmatism as the guyot has moved away from the hotspot (Fig. 10a; Sano and Kanmera, 1991; Kusky et al., 2013). Large amounts of colluvial conglomerate form on the margins of ocean islands, with clasts and matrix dominated by poorly-sorted limestone and basalt clasts (Fig. 10a). Cherts form at the base of the ocean island (Fig. 10a). It is expected that terrigenous material (e.g., quartz) is absent from sedimentary and pyroclastic rocks that form far from continental margins (Fig. 10a; Sano and Kanmera, 1991; Kusky et al., 2013).

An alternative to the Hawaiian model is provided by ocean islands such as Cape

Verde and Selvagen within the Atlantic Ocean, which form on slow moving or near-stationary plates (Ramalho et al., 2010a). Here their formation is conceptualized as the Cape Verde model. During formation of these islands, the slow or near-stationary plate permits volcanic islands to remain close to hotspot centers over long periods of time, so that alternating basaltic magmatism and limestone deposition results in basalt intercalated with limestone and pyroclastic rock layers (Fig. 10b; Robertson et al., 1984; Geldmacher et al., 2001; Dyhr and Holm, 2010; Ramalho et al., 2010b). Trachyandesite, trachyte, and phonolite are found within modern ocean island sequences (e.g., Hawaii, Samoa, Azores, and Cape Verde; Geldmacher et al., 2001; Beier et al., 2007; Ramalho et al., 2010a; Mourão et al., 2012; Haase et al., 2019).

In summary, the thick basaltic basement covered by limestone, limestone interbedded with basalt and tuff, marginal colluvial conglomerates, and chert, in association with the absence of terrigenous material (e.g., quartz) from the limestone, colluvial conglomerate, and pyroclastic rocks, are characteristic features of ocean island sequences (Figs. 10a–10b).

Ocean island-like sequences formed in collisional settings

Ocean island-like sequences in collisional settings form within post-collisional submarine basins on continental crust (Zhu et al., 2016; Li et al., 2019a), and it is difficult to reconcile the existence of thick basaltic basement and a cover sequence of related colluvial conglomerate with the features of this setting. Uplifted orogenic belts typically surround post-collisional submarine basins, and the uplifted rocks provide terrigenous clasts that are preserved within sedimentary rocks (e.g., limestone and conglomerate). Typically, Ti-rich alkaline basalts interbedded with terrigenous sandstones, siltstones, and shales form in this setting (Sutton, 1978; Soesoo et al., 1997). These rocks differ from ocean island sequences, which lack terrigenous clasts (Figs. 10a–10b).

Zhonggang igneous–sedimentary rocks: Remnants of a typical Cape Verde-type ocean island within the Meso-Tethys Ocean

The Zhonggang igneous–sedimentary rocks comprise a thick basaltic basement covered by limestones with interbedded basalts and tuffs (Figs. 2d, 3a–3c), and a characteristic colluvial conglomerate (Fig. 3g). These rocks resemble modern Cape Verde-type ocean island sequences (Fig. 10b; Robertson et al., 1984; Geldmacher et al., 2001; Dyhr and Holm, 2010; Ramalho et al., 2010b). The absence of terrigenous clasts (e.g., quartz) from the limestone, colluvial conglomerate, and tuff (Figs. 4c–4f) is inconsistent with the collisional model, but supports the ocean island model. We therefore infer that the Zhonggang igneous–sedimentary rocks are remnants of a Cape Verde-type ocean island. Further support for this inference is provided by the following two lines of evidence.

(1) Ocean islands that form within deep ocean basins accrete onto the accretionary wedge as exotic blocks within a matrix of flysch deposits during subduction of oceanic lithosphere. In contrast, ocean island-like sequences produced in collisional settings form after the accretionary wedge, so they typically occur above

the accretionary wedge after collision. The widespread occurrence of exotic block-in-matrix structures on contacts between the Zhonggang igneous–sedimentary rocks and the flysch deposits (Figs. 3h–3i) provide strong evidence that the Zhonggang igneous–sedimentary rocks are ocean island remnants.

(2) All of the Zhonggang basalts and trachyandesites are enriched in LREE (Figs. 6a, 6c), and have positive Nb–Ta anomalies (Figs. 6b, 6d). They are derived from a garnet-facies mantle source, and the ascending magmas were not contaminated by the crust (Figs. 9a–9b). These characteristics are similar to those of igneous rocks from modern intraplate ocean islands (Sun and McDonough, 1989; Niu et al., 2011; Haase et al., 2019). Furthermore, the whole-rock Sr–Nd isotopic compositions of the Zhonggang igneous rocks are similar to those of igneous rocks from modern intraplate ocean islands (e.g., Cape Verde and Azores, Atlantic Ocean; Figs. 8, 11; Widom et al., 1997; Pfänder et al., 2007; Tanaka et al., 2008; Niu et al., 2011; Garapić et al., 2015; Mata et al., 2017).

In summary, we infer that the Zhonggang igneous–sedimentary rocks are remnants of a typical Cape Verde-type ocean island that formed within the deep ocean basin of the Meso-Tethys Ocean (Fig. 11).

Timing of closure of the Meso-Tethys Ocean

The Zhonggang igneous–sedimentary rocks are remnants of a typical Cape Verde-type ocean island that formed at 141–135 Ma, which indicates that the Meso-Tethys Ocean was still opening at this time (Fig. 12a). Therefore, final closure of the Meso-Tethys Ocean and the subsequent Lhasa–Qiangtang continental collision must have occurred after ca. 135 Ma. Furthermore, we infer that the final closure of the Meso-Tethys Ocean was diachronous from east to west during the late Early Cretaceous (130–100 Ma; Fig. 12b; Fan et al., 2018a), based on paleomagnetic data showing that north-directed movement of the Lhasa Terrane ceased by ca. 132 Ma (Ma et al., 2018), the transition from marine to non-marine environments occurred at 125–118 Ma within the Nyima area of the Lhasa Terrane (Fig. 1b; Kapp et al., 2007), and continental fluvial–lacustrine strata and a related angular unconformity formed within the BNSZ and surrounding areas at 118–92 Ma (118–113 Ma within Baingoin in the east, 108–103 Ma within Gerze in the center, and 96–92 Ma within Ritu in the west; Fig. 1b; Li et al., 2016; Hu et al., 2017; Fan et al., 2018a; Zhu et al., 2019; Lai et al., 2019). However, if the Meso-Tethys Ocean closed during the late Early Cretaceous (130–100 Ma), the Middle Jurassic (ca. 166 Ma) and the latest Jurassic (ca. 145 Ma) geological events in the BNSZ and southern Qiangtang Terrane must be considered.

The unconformity and associated provenance changes that support an event at ca. 166 Ma are recorded from the Amdo region, where the Amdo microcontinent and associated gneiss underwent amphibolite- to granulite-facies metamorphism at 190–170 Ma (Guynn et al., 2006; Zhang et al., 2014b). Some researchers have linked the ca. 166 Ma event to the Amdo–Qiangtang collision (Zhu et al., 2016; Hao et al., 2019; Li et al., 2019b). Some researchers also argued that the ca. 166 Ma event may be associated with the accretion of the ca. 185 Ma oceanic plateau (Zhang et al., 2014a) onto the southern Qiangtang continental margin (Yan and Zhang, 2020), or ridge subduction (Li et al., 2020). Combined with the 141–135 Ma ocean island revealed by this study (Fig. 12a) and the 169–148 Ma ophiolitic mélange near the Amdo region (Zhong et al., 2017; Tang et al., 2020), we conclude that the ca. 166 Ma event was more likely related to the subduction of microcontinent, oceanic plateau or ocean ridge within the Meso-Tethys Ocean, rather than the Lhasa-Qiangtang collision.

As for the ca. 145 Ma event, we proposed it is associated with subduction of a Jurassic intra-oceanic arc, rather than the Lhasa-Qiangtang collision. Remnants of this Jurassic intra-oceanic arc within the Meso-Tethys Ocean extend eastwards for ~1500 km through the Ritu, Julu, Zhongcang, Dongco, Baingoin areas, and into the Naqu area (Tang et al., 2019; Fan et al., 2019; Yan and Zhang, 2020). The intra-oceanic arc might have initially formed at ca. 180 Ma (Fan et al., 2019; Li et al., 2019b), and evolved during 172–162Ma (Shi et al., 2008; Liu et al., 2014; Zeng et al., 2016; Huang et al., 2017; Tang et al., 2019; Fan et al., 2019; Yan and Zhang, 2020).

The 160–155 Ma granodiorites were emplaced directly onto 180–162 Ma intra-oceanic arc sequences within the Dongco area (Fig. 2a). The granodiorites contain large numbers of inherited zircons with similar age spectra to those of detrital zircons within the surrounding graywackes of the accretionary wedge, suggesting that many of these graywackes were assimilated during formation of the 160–155 Ma Dongco granodiorites (Fan et al., 2016). Relationships amongst the 160–155 Ma Dongco granodiorites, 180–162 Ma intra-oceanic arc, and accretionary wedge indicate that the 180–162 Ma intra-oceanic arc was accreting, or had accreted, onto the accretionary wedge during the Late Jurassic (160–155 Ma). Subsequent Late Jurassic–Early Cretaceous (150–130 Ma) subduction of the intra-oceanic arc might have occurred, causing the ca. 145 Ma geological event (Fig. 12a) in central Tibet. In addition, subduction of an intra-oceanic arc, which has a greater height and buoyancy than oceanic crust, commonly chokes the receiving subduction zone (Hawkins et al., 1984; Mann and Taira, 2004; Chen et al., 2018), which slows or stops movement of the subducting plate (Fig. 12a). The 141–135 Ma Zhonggang igneous–sedimentary rocks are remnants of a typical Cape Verde-type ocean island that formed on a slow-moving or near-stationary plate within the Meso-Tethys Ocean, which provides further evidence for subduction of an intra-oceanic arc at 150–130 Ma (Fig. 12a).

CONCLUSIONS

(1) The Zhonggang igneous–sedimentary rocks formed at 141–135 Ma, and are remnants of a Cape Verde-type ocean island formed within the deep ocean basin of the Meso-Tethys Ocean. They provide strong evidence that the Meso-Tethys Ocean was still opening at ca. 135 Ma.

(2) Final closure of the Meso-Tethys Ocean and the Lhasa–Qiangtang collision might have been diachronous, from east to west, during the late Early Cretaceous (130–100 Ma).

ACKNOWLEDGMENTS

This research was supported by the National Science Foundation of China (Grant No. 41972236，41702227), the Second Tibetan Plateau Scientific Expedition and Research (STEP) Program (grant 2019QZKK0703), and Self-determined Foundation of Key Laboratory of Mineral Resources Evaluation in Northeast Asia, Ministry of Natural Resources of China (DBY-ZZ-18-04). All data are provided in the supporting information, and are available at http://dx.doi.org/10.17632/kk5n8wcrth.1 (DOI: 10.17632/kk5n8wcrth.1).

REFERENCES CITED

Akal, C., Candan, O., Koralay, O.E., Oberhansli, R., Chen, F., and Prelevic, D., 2012, Early Triassic potassic volcanism in the Afyon Zone of the Anatolides/Turkey: implications for the rifting of the Neo-Tethys: International Journal of Earth Sciences, v. 101, p. 177–194.

Aldanmaz, E., Pearce, J.A., Thirlwall, M.F., and Mitchell, J.G., 2000, Petrogenetic evolution of late Cenozoic post–collision volcanism in western Anatolia, Turkey: Journal of Volcanology and Geothermal Research, v. 102, p. 67–95.

Allègre, C.J., Courtillot, V., Tapponnie, P., and other 32 co–authors., 1984, Structure and evolution of the Himalaya–Tibet orogenic belt: Nature, v. 307, p. 17–22.

Bao, P. S., Xiao, X.C., Su, L., and Wang, J., 2007, Petrological, geochemical and chronological constraints for the tectonic setting of the Dongco ophiolite in Tibet: Science China-Earth Sciences, v. 50, p. 660–671.

Beier, C., Stracke, A., and Haase, K.M., 2007, The peculiar geochemical signatures of

São Miguel (Azores) lavas: Metasomatised or recycled mantle sources? Earth and Planetary Science Letters, v. 259, p. 186–199.

Belousova, E., Griffin, W., O'Reilly, S.Y., and Fisher, N., 2002, Igneous zircon: trace element composition as an indicator of source rock type: Contributions to Mineralogy and Petrology, v. 143, p. 602–622.

Chen, G.R., Liu, H.F., Jiang, G.W., Zeng, Q.G., Zhao, S.R., and Zhang, X.G., 2004, Discovery of the Shamuluo formation in the central segment of the Bangong Co-Nujiang River suture zone, Tibet: Geological Bulletin of China, v. 23, p. 193–194 (In Chinese with English abstract).

Chen, S. S., Shi, R.D., Zou, H.B., Huang, Q.S., Liu, D.L., Gong, X.H., Yi, G.D., and Wu, K., 2015, Late Triassic island-arc–back-arc basin development along the Bangong–Nujiang suture zone (central Tibet): Geological, geochemical and chronological evidence from volcanic rocks: Lithos, v. 230, p. 30–45.

Chen, S.S., Shi, R.D., Fan, W.M., Gong, X.H., and Wu, K., 2017, Early Permian mafic dikes in the Nagqu area, Central Tibet, China, associated with embryonic oceanic crust of the Meso-Tethys Ocean: Journal of Geophysical Research: Solid Earth, v. 122, p. 4172–4190.

Chen, W.Y., Hu, X.C., Zhong, Y., Fu, Y.B., Li, F., and Wang, Y.G., 2018, Comment on “Sedimentary and tectonic evolution of the southern Qiangtang basin: Implications for the Lhasa-Qiangtang collision timing” by A. Ma et al. Journal of Geophysical Research: Solid Earth, v. 123, p. 7338–7342.

Condie, K.C., 1993, Chemical composition and evolution of the upper continental crust: Contrasting results from surface samples and shales: Chemical Geology, v. 104, p. 1–37.

Darwin, C., 1842, On the Structure and Distribution of Coral Reefs: Ward Lock, London, UK.

Detrick, R., and Crough, T., 1978, Island subsidence, hot spots, and lithospheric thinning: Journal of Geophysical Research: Solid Earth, v. 83, p. 1236–1244.

Dyhr, C., and Holm, P., 2010, A volcanological and geochemical investigation of Boa Vista, Cape Verde Islands; $^{40}Ar/^{39}Ar$ geochronology and field constraints: Journal of Volcanology and Geothermal Research, v. 189, p. 19–32.

Ellam, 1992, Lithospheric thickness as a control on basalt geochemistry: Geology, v. 20, p. 153-156.

Elliott, T., Blichert-Toft, J., Heumann, A., Koetsier, G., and Forjaz, V., 2007, The origin of enriched mantle beneath São Miguel, Azores: Geochimica et Cosmochimica Acta, v. 71, p. 219–240.

Fan, J.J., Li, C., Xie, C.M., and Wang, M., 2014, Petrology, geochemistry, and geochronology of the Zhonggang ocean island, northern Tiber: implications for the evolution of the Bangongco–Nujiang oceanic arm of Neo–Tethys: International Geology Review, v. 56, p. 1504–1520.

Fan, J. J., Li, C., Xie, C.M., Wang, M., and Chen, J.W., 2015, Petrology and U-Pb zircon geochronology of bimodal volcanic rocks from the Maierze Group, northern Tibet: Constraints on the timing of closure of the Banggong-Nujiang Ocean: Lithos, v. 227, p. 148–160.

Fan, J.J., Li, C., Wu, H., Zhang, T.Y., Wang, M., Chen, J.W., and Xu, J.X., 2016, Late Jurassic adakitic granodiorite in the Dong Co area, northern Tibet: Implications for subduction of the Bangong–Nujiang oceanic lithosphere and related accretion of the Southern Qiangtang terrane: Tectonophysics, v. 691, p. 345–361.

Fan, J.J., Li, C., Wang, M., Liu, Y.M., and Xie, C.M., 2017, Remnants of a Late Triassic ocean island in the Gufeng area, northern Tibet: Implications for the opening and early evolution of the Bangong–Nujiang Tethyan Ocean: Journal of Asian Earth Sciences, v. 135, p. 35–50.

Fan, J.J., Li, C., Wang, M., Xie, C.M., 2018a, Reconstructing in space and time the closure of the middle and western segments of the Bangong–Nujiang Tethyan Ocean in the Tibetan Plateau: International Journal of Earth Sciences, v. 107, p. 231–249.

Fan, J.J., Li, C., Liu, J.H., Wang, M., Liu, Y.M., and Xie, C.M., 2018b, The Middle Triassic evolution of the Bangong–Nujiang Tethyan Ocean: evidence from analyses of OIB-type basalts and OIB-derived phonolites in northern Tibet: International Journal of Earth Sciences, v. 107, p. 1755–1775.

Fan, J.J., Zhang, B.C., Liu, H.Y., Liu, Y.M., Yu, Y.P., Hao, Y.J., and Danzeng, A.W., 2019, Early-Middle Jurassic intra-oceanic subduction of the Bangong-Nujiang oceanic lithosphere: Evidence of the Dong Co ophiolite: Acta Petrologica Sinica, v. 35, p. 3048–3064 (in Chinese with English abstract).

Feng, G., Liu, S., Feng, C., Yang, Y., Yang, C., Tang, L., and Yang, J., 2015, U–Pb zircon geochronology, geochemistry and geodynamic significance of basaltic trachyandesites and trachyandesites from the Jianchang area, western Liaoning Province, China: Journal of Asian Earth Sciences, v. 110, p. 141–150.

Garapić, G., Jackson, M.G., Hauri, E.H., Hart, S.R., Farley, K.A., Blusztajn, J.S., and Woodhead, J.D., 2015, A radiogenic isotopic (He-Sr-Nd-Pb-Os) study of lavas from the Pitcairn hotspot: Implications for the origin of EM-1 (enriched mantle 1): Lithos, v. 228–229, p. 1–11.

Geldmacher, J., Hoernle, K., van den Bogaard, P., Zankl, G., and Garbe-Schonberg, D., 2001, Earlier history of the ≥70-Ma-old Canary hotspot based on the temporal and geochemical evolution of the Selvagen Archipelago and neighboring seamounts in the eastern North Atlantic: Journal of Volcanology and Geothermal Reseach, v. 111, p. 55–87.

Geng, Q., Zhang, Z., Peng, Z., Guan, J., Zhu, X., and Mao, X., 2016, Jurassic–Cretaceous granitoids and related tectono-metallogenesis in the Zapug-Duobuza arc, western Tibet: Ore Geology Reviews, v. 77, p. 163–175.

Girardeau, J., Marcoux, J., Allegre, C., Bassoullet, J., Youking, T., Xuchang, X., Yougong, Z., and Xibin, W., 1984, Tectonic environment and geodynamic signifcance of the NeoCimmerian Donqiao ophiolite, Bangong-Nujiang suture zone, Tibet: Nature, v. 307, p. 27.

Grigg, R., 1982, Darwin Point: a threshold for atoll formation: Coral Reefs, v. 1, p. 29–34.

Guynn, J., Kapp, P., Pullen, A., Heizler, M., Gehrels, G., and Ding, L., 2006, Tibetan basement rocks near Amdo reveal “missing” Mesozoic tectonism along the

Bangong suture, central Tibet: Geology, v. 34, p. 505–508.

Haase, K.M., Beier, C., and Kemner, F., 2019, A Comparison of the Magmatic Evolution of Pacific Intraplate Volcanoes: Constraints on Melting in Mantle Plumes: Frontiers in Earth Science, v. 6, p. 242.

Hao, L.L., Wang, Q., Zhang, C., Qu, Q., Yang, J.H., Dan, W., and Jiang, Z.Q., 2019, Oceanic plateau subduction during closure of the Bangong-Nujiang Tethyan Ocean: Insights from central Tibetan volcanic rocks: Geological Society of America Bulletin, v. 131, p. 864–880.

Hart, S.R., and Staudigel, H., 1982, The control of alkalies and uranium in seawater by ocean crust alteration: Earth and Planetary Science Letters, v. 58, p. 202–212.

Hart, S.R., and Dunn, T., 1993, Experimental cpx/melt partitioning of 24 trace elements: Contributions to Mineralogy and Petrology, v. 113, p. 1–8.

Hauri, E.H., Wagner, T.P., and Grove, T.L., 1994, Experimental and natural partitioning of Th, U, Pb and other trace elements between garnet. clinopyroxene and basaltic melts: Chemical Geology, v. 117, p. 149–166.

Hawkins, J.W., Bloomer, S.H., Evans, C.A., Melchior, J.T., 1984, Evolution of intra-ceanic arc-trench systems: Tectonophysics, v. 102, p. 175–205.

Horn, I., Foley, S.F., Jackson, S.E., and Jenner G.A., 1994, Experimentally determined partitioning of high field strength and selected transition elements between spinel and basaltic melt: Chemical Geology, v. 117, p. 193–218

Hoskin, P.W.O., and Schaltegger, U., 2003, The Composition of Zircon and Igneous and Metamorphic Petrogenesis: Mineralogical Society of America, Washington, DC, p. 36 ETATS-UNIS.

Hu, P.Y., Li, C., Wu, Y.W., Xie, C.M., Wang, M., and Li, J., 2014, Opening of the Longmu Co–Shuanghu–Lancangjiang ocean: constraints from plagiogranites: Chinese Science Bulletin, v. 59, P. 3188–3199.

Hu, P.Y., Zhai, Q.G., Jahn, B.M., Wang, J., Li, C., Lee, H.Y., and Tang, S.H., 2015, Early Ordovician granites from the South Qiangtang terrane, northern Tibet: Implications for the early Paleozoic tectonic evolution along the Gondwanan proto-Tethyan margin: Lithos, v. 220-223, p. 318–338.

Hu, P.Y., Zhai, Q.G., Jahn, B.M., Wang, J., Chung, S.L., Lee, H.Y., and Tang, S.H., 2017, Late Early Cretaceous magmatic rocks (118–113 Ma) in the middle segment of the Bangong–Nujiang suture zone, Tibetan Plateau: Evidence of lithospheric delamination: Gondwana Research, v. 44, p. 116–138.

Hu, P.Y., Zhai, Q.G., Zhao, G.C., Wang, J., Tang, Y., Wang, H.T., Zhu, Z.C., Wu, H., Wang, W., 2019, Late Cryogenian magmatic activity in the North Lhasa terrane, Tibet: Implication of slab break-off process: Gondwana Research, v. 71, p. 129–149.

Huang, Q.T., Liu, W.L., Xia, B., Cai, Z.R., Chen, W.Y., Li, J.F., and Yin, Z.X., 2017, Petrogenesis of the Majiari ophiolite (western Tibet, China): Implications for intra-oceanic subduction in the Bangong-Nujiang Tethys: Journal of Asian Earth Sciences, v. 146, p. 337-351.

Huang, T.T., Xu, J.F., Chen, J.L., Wu, J.B., and Zeng, Y.C., 2017, Sedimentary record of Jurassic northward subduction of the Bangong–Nujiang Ocean: insights from detrital zircons: International Geology Review, v. 59, p. 166–184.

Johnson, K.T.M., 1994, Experimental cpx/ and garnet/melt partitioning of REE and other trace elements at high pressures: petrogenetic implications: Mineralogical Magazine, v. 58, p. 454–455.

Kapp, P., and DeCelles, P.G., 2019, Mesozoic–Cenozoic geological evolution of the Himalayan-Tibetan orogen and working tectonic hypotheses: American Journal of Science, v. 319, p. 159–254.

Kapp, P., DeCelles, P.G., Gehrels, G.E., Heizler, M., and Ding, L., 2007, Geological records of the Lhasa–Qiangtang and Indo–Asian collisions in the Nima area of central Tibet: Geological Society of America Bulletin, v. 119, p. 917–932.

Kusky, T.M., Windley, B.F., Safonova, I., Wakita, K., Wakabayashi, J., Polat, A., Santosh, M., 2013, Recognition of ocean plate stratigraphy in accretionary orogens through Earth history: A record of 3.8 billion years of sea floor spreading, subduction, and accretion: Gondwana Research, v. 24, p. 501–547.

Lai, W., Hu, X. M, Garzanti, E., Sun, G. Y, Garzione, C. N., Fadel, M. B., and Ma, A.L, 2019, Initial growth of the northern Lhasaplano, Tibetan Plateau in the early Late Cretaceous (ca. 92 Ma). Geological Society of America Bulletin, v. 131, p.1823–1836.

Li, H.L., Gao, C., Li, Z.H., Zhang, Z., Peng, Z.M., and Guan, J.L., 2016, Age and Tectonic Significance of Jingzhushan Formation in Bangong Lake Area, Tibet: Geotectonica et Metallogenia, v. 40, p. 663–673 (in Chinese with English abstract).

Li, J.X., Qin, K.Z., Li, G.M., Richards, J.P., Zhao, J.X., and Cao, M.J., 2014a.

Geochronology, geochemistry, and zircon Hf isotopic compositions of Mesozoic intermediate– felsic intrusions in central Tibet: petrogenetic and tectonic implications: Lithos, v. 198–199, p. 77–91.

Li, S., Yin, C., Guilmette, C., Ding, L., and Zhang, J., 2019a. Birth and demise of the Bangong-Nujiang Tethyan Ocean: A review from the Gerze area of central Tibet: Earth-Science Reviews, v. 198, p. 102907.

Li, S., Guilmette, C., Yin, C., Ding, L., Zhang, J., Wang, H., and Baral, U., 2019b. Timing and mechanism of Bangong-Nujiang ophiolite emplacement in the Gerze area of central Tibet: Gondwana Research, v. 71, p. 179–193.

Li, S.M., Wang, Q., Zhu, D.C., Cawood, P.A., Stern, R.J., Weinberg, R., Zhao, Z.D., and Mo, X.X., 2020, Reconciling Orogenic Drivers for the Evolution of the Bangong-Nujiang Tethys During Middle-Late Jurassic: Tectonics, v. 39, p. e2019TC005951.

Li, X.K., Chen, J., Wang, R.C., and Li, C., 2018, Temporal and spatial variations of Late Mesozoic granitoids in the SW Qiangtang, Tibet: Implications for crustal architecture, Meso-Tethyan evolution and regional mineralization: Earth-Science Review, v. 185, p. 374–396.

Liu, C.Z., Chung, S.L., Wu, F.Y., Zhang, C., Xu, Y., Wang, J.G., Chen, Y., and Guo, S., 2016, Tethyan suturing in Southeast Asia: Zircon U-Pb and Hf-O isotopic constraints from Myanmar ophiolites: Geology, v. 44, p. 311–318.

Liu, D., Shi, R., Ding, L., Huang, Q., Zhang, X., Yue, Y., and Zhang, L., 2017, Zircon U–Pb age and Hf isotopic compositions of Mesozoic granitoids in southern

Qiangtang, Tibet: Implications for the subduction of the Bangong–Nujiang Tethyan Ocean: Gondwana Research, v. 41, p. 157–172.

Liu, K., Wilde, S.A., Zhang, J., Xiao, W., Wang, M., and Ge, M., 2020, Zircon U–Pb dating and whole-rock geochemistry of volcanic rocks in eastern Heilongjiang Province, NE China: Implications for the tectonic evolution of the Mudanjiang and Paleo-Pacific oceans from the Jurassic to Cretaceous: Geological Journal v. 55, p. 1866–1889.

Liu, W.L., Huang, Q.T., Gu, M., Zhong, Y., Zhou, R., Gu, X.D., Zheng, H., Liu, J.N., Lu, X.X., and Xia, B., 2018, Origin and tectonic implications of the Shiquanhe high-Mg andesite, western Bangong suture, Tibet: Gondwana Research, v. 60, p. 1–14.

Liu, W.L., Xia, B., Zhong, Y., Cai, J.X., Li, J.F., Liu, H.F., Cai, Z.R., and Sun, Z.L., 2014, Age and composition of the Rebang Co and Julu ophiolites, central Tibet: Implications for the evolution of the Bangong Meso-Tethys: International Geology Review, v. 56, p. 430–447.

Ma, A., Hu, X., Garzanti, E., Han, Z., and Lai, W., 2017, Sedimentary and tectonic evolution of the southern Qiangtang basin: Implications for the LhasaQiangtang collision timing: Journal of Geophysical Research: Solid Earth, v. 122, p. 4790–4813.

Ma, Y., Yang, T., Bian, W., Jin, J., Wang, Q., Zhang, S., Wu, H., Li, H., Cao, L., 2018. A stable southern margin of Asia during the Cretaceous: Paleomagnetic constraints on the Lhasa-Qiangtang collision and the maximum width of the

Neo-Tethy: Tectonics, v. 37, p. 3853-3876.

Mann, P., and Taira, A., 2004, Global tectonic significance of the Solomon Islands and Ontong Java Plateau convergent zone: Tectonophysics, v. 389, p. 137–190.

Mata, J., Martins, S., Mattielli, N., Madeira, J., Faria, B., Ramalho, R.S., Silva, P., Moreira, M., Calderia, R., Moreira, M., Rodrigues, J., and Martins, L., 2017, The 2014–15 eruption and the short-term geochemical evolution of the Fogo volcano (Cape Verde): Evidence for small-scale mantle heterogeneity: Lithos v. 288–289, p. 91–107.

McKenzie, D., and OpNions, R.K., 1991, Partial melt distributions from inversion of rare Earth element concentrations: Journal of Petrology, v. 32, p. 1021–1091.

Mclelland, J.M., Daly, J.S., and Chiarenzelli, J., 1993, Sm-Nd and U-Pb Isotopic Evidence of Juvenile Crust In the Adirondack Lowlands and Implications for the Evolution of the Adirondack Mts. Journal of Geology, v. 101, p. 97–105.

Menard, H., 1983. Insular erosion, isostasy, and subsidence: Science, v. 220, p. 913–918.

Menard, H., and Ladd, H., 1963, Oceanic islands, seamounts, guyots and atolls: The sea, v. 3, p. 365–385.

Meng, F.X., Gao, S., Niu, Y.L., Liu, Y.S., and Wang, X.R., 2015, Mesozoic–Cenozoic mantle evolution beneath the North China Craton: a new perspective from Hf–Nd isotopes of basalts: Gondwana Research, v. 27, p. 1574–1585.

Metcalfe, I., 2013, Gondwana dispersion and Asian accretion: tectonic and palaeogeographic evolution of eastern Tethys: Journal of Asian Earth Sciences, v.

66, p. 1–33.

Morgan, J., Morgan, W., and Price, E., 1995, Hotspot melting generates both hotspot volcanism and a hotspot swell: Journal of Geophysical Research: Solid Earth, v. 100, p. 8045–8062.

Mourão, C., Mata, J., Doucelance, R., Madeira, J., Millet, M.A., and Moreita, M., 2012, Geochemical temporal evolution of Brava Island magmatism: Constraints on the variability of Cape Verde mantle sources and on carbonatite–silicate magma link: Chemical Geology, v. 334, p. 44–61.

Niu, Y., Wilson, M., Humphreys, E.R., and O'Hara, M.J., 2011, The Origin of Intra-plate Ocean Island Basalts (OIB): the Lid Effect and its Geodynamic Implications: Journal of Petrology, v. 52, p. 1443–1468.

Niu, Y.L., 2009, Some basic concepts and problems on the petrogenesis of intra-plate ocean island basalts: Chinese Science Bulletin, v. 54, p.418–4160.

Oyan, V., Keskin, M., Lebedev, V.A., Chugaev, A.V., Sharkow, E.V., and Unal, E., 2017, Petrology and geochemistry of the Quaternary mafic volcanism to the NE of Lake Van, Eastern Anatolian Collision Zone, Turkey: Journal of Petrology, v. 58, p. 1701-1728.

Pan, G.T., Wang, L.Q., Li, R.S., Yuan, S.H., Ji, W.H., Yin, F.G., Zhang, W.P., and Wang, B.D., 2012, Tectonic evolution of the Qinghai–Tibet Plateau: Journal of Asian Earth Sciences, v. 53, p. 3–14.

Pfänder, J.A., Münker, C., Stracke, A., and Mezger, K., 2007, Nb/Ta and Zr/Hf in ocean island basalts–Implications for crust–mantle differentiation and the fate of

Niobium: Earth and Planetary Science Letters, v. 254, p. 158–172.

Ramalho, R.S., Helffrich, G., Cosca, M., Vance, D., Hoffmann, D., and Schmidt, D.N., 2010a, Vertical movements of ocean island volcanoes: Insights from a stationary plate environment: Marine Geology, v. 275, p. 84–95.

Ramalho, R., Helffrich, G., Schmide, D., Vance, D., 2010b, Tracers of uplift and subsidence in the Cape Verde Archipelago: Journal of the Geological Society, v. 167, p. 519–538.

Robertson, 1984, Mesozoic deep-water and Tertiary volcaniclastic deposition of Maio, Cape Verde Islands: Implications for Atlantic paleoenvironments and ocean island volcanism: Geological Society of America Bulletin, v. 95, p. 433–453.

Rudnick, R.L., Gao, S., 2003, Composition of the continental crust: Treatise on Geochemistry, v. 3, p. 1–64.

Samson, S.D., Hibbard, J.P., and Wortman, G.L., 1995, Nd isotopic evidence for juvenile crust in the Carolina terrane, southern Appalachians: Contributions to Mineralogy and Petrology, v. 121, p. 171–184.

Sano, H., Kanmera, K., 1991, Collapse of ancient oceanic reef complex–what happened during collision of Akiyoshi reef complex? Sequence of collisional collapse and generation of collapse products: Journal of the Geological Society of Japan v. 97, p. 631–644.

Schwandt, C.S., McKay, G.A., 1998, Rare earth element partition coefficients from enstatite/melt synthesis experiments: Geochimica et Cosmochimica Acta, v. 62, p. 2845–2848.

Shi, R. D., Griffin, W.L., O'Reilly, S.Y., Huang, Q.S., Zhang, X.R., Liu, D.L., Zhi, X.C., Xia, Q.X., and Ding, L., 2012, Melt/mantle mixing produces podiform chromite deposits in ophiolites: Implications of Re–Os systematics in the Dongqiao Neo-Tethyan ophiolite, northern Tibet: Gondwana Research, v. 21, p. 194–206.

Shi, R.D., Yang, J.S., Xu, Z.Q., and Qi, X.X., 2008, The Bangong Lake ophiolite (NW Tibet) and its bearing on the tectonic evolution of the Bangong–Nujiang suture zone: Journal of Asian Earth Sciences, v. 32, p. 438–457.

Shu, X., Yang, S.Y., Jiang, S.Y., and Ye, M., 2017, Petrogenesis and geodynamic setting of Early Cretaceous felsic rocks in the Gan-Hang Belt, Southeast China: Constraints from geochronology and geochemistry of the tuffs and trachyandesitic rocks in Shengyuan volcanic Basin: Lithos, v. 284-285, p. 691–708.

Soesoo, A., Bons, P.D., Gray, D.R., and Foster, D.A., 1997, Divergent double subduction: tectonic and petrologic consequences: Geology v. 25, p. 755–758.

Sun, S.S., and McDonough, W.F., 1989, Chemical and isotope systematics of oceanic basalts: implications for mantle composition and processes. In: Saunders A D (eds.), Magmatism in ocean Basins. Geological Society Publication, v. 42, p. 313–345.

Sutton, G., 1978, Snowy Bluff volcanics and Red Bed sediments of the Avon River group [B.Sc. thesis]: Clayton, Victoria, Australia, Monash University, p. 89.

Tanaka, R., Makishima, A., and Nakamura, E., 2008, Hawaiian double volcanic chain triggered by an episodic involvement of recycled material: Constraints from temporal Sr–Nd–Hf–Pb isotopic trend of the Loa-type volcanoes: Earth and Planetary Science Letters, v. 265, p. 450–465.

Tang, H., Zheng, J., Griffin, W.L., Su, Y., Yu, C., and Ren, H., 2012, U-Pb zircon geochronology, geochemistry and geodynamic significance of basaltic trachyandesites and trachyandesites from the Jianchang area, western Liaoning Province, China: Precambrian Research, v. 220-221, p. 91–106.

Tang, Y., Zhai, Q.G., Chung, S.L., Hu, P.Y., Wang, J., Xiao, X.C., Song, B., Wang, H.T., and Lee, H.Y., 2020, First mid-ocean ridge-type ophiolite from the Meso-Tethys suture zone in the north-central Tibetan plateau: Geological Society of America Bulletin, doi: 10.1130/B35500.1.

Tang, Y., Zhai, Q.G., Hu, P.Y., Xiao, X.C., and Wang, H.T., 2019, Petrology, geochemistry and geochronology of the Zhongcang ophiolite, northern Tibet: Implications for the evolution of the Bangong-Nujiang Ocean: Geoscience Frontiers, v. 9, p. 1369–1381.

Thorpe, R.S., Potts, P.J., and Francis, P.W., 1976, Rare Earth Data and Petrogenesis of Andesite from the North Chilean Andes: Contributions to Mineralogy and Petrology, v. 54, p. 65–78.

Verma, S.P., 1981, Seawater alteration effects on 87Sr/86Sr, K, Rb, Cs, Ba and Sr in oceanic igneous rocks: Chemical Geology, v. 34, p. 81–89.

Wang, B.D., Wang, L.Q., Chung, S.L., Chen, J.L., Yin, F.G., Liu, H., Li, X.B., and Chen, L.X., 2016, Evolution of the Bangong–Nujiang Tethyan ocean: Insights from the geochronology and geochemistry of mafic rocks within ophiolites: Lithos, v. 245, p. 18–33.

Wang, C.G., Sun, F.Y., Sun, G.S., Li, Y., Sun, J.D., and Feng, H.D., 2016, Zircon U–Pb Geochronology, Elemental Geochemistry and Geological Implications of the Andesite of the Yixian Formation in the Tiejiangyingzi Basin in Southeastern Chifeng, China: Resource Geology v. 66, p. 149–162.

Wang, M. Z., and Dong, D.Y., 1984, Stromatoporoids from the Dongqiao formation (Upper Jurassic-Lower Cretaceous) in northern Xizang (Tibet): Acta Palaeontologica Sinica, v. 12, p. 343–352 (in Chinese with English abstract).

Wei, S.G., Song, Y., Tang, J.X., Liu, Z.B., Wang, Q., Gao, K., Li, Z., and Li, F.Q., 2019, Zircon U-Pb age, geochemistry and Sr-Nd isotope characteristics of the Duolong SSZ-type ophiolites in Gaize County, Tibet: Evidence for intra-oceanic subduction of the Bangonghu-Nujiang Ocean during the Late Permian: Acta Petrologica Sinica, v. 35, p. 505–522 (in Chinese with English abstract).

Widom, E., Carlson, R.W., Gill, J.B., Schmincke, H.-U., 1997, Th–Sr–Nd–Pb isotope and trace element evidence for the origin of the Sao Miguel, Azores, enriched mantle source: Chemical Geology, v. 140, p. 49–68.

Winchester, J.A., and Flody, P.A., 1977, Geochemical magma type discrimination: application to altered and metamorphosed basic igneous rocks: Earth and Planetary Science Letters, v. 28, p. 459–469.

Wu, H., Sun, S., Liu, H., Chu, H., and Ding, W., 2018, An Early Cretaceous slab window beneath central Tibet, SW China: Evidence from OIB-like alkaline gabbros in the Duolong area: Terra Nova, v. 31, p. 67–75.

Xu, Z., Dilek, Y., Cao, H., Yang, J., Robinson, P., Ma, C., Li, H., Jolivet, M., Roger, F., and Chen, X., 2015, Paleo-Tethyan evolution of Tibet as recorded in the East Cimmerides and West Cathaysides: Journal of Asian Earth Sciences, v. 105, p. 320–337.

Xu, Z.T., Sun, J.G., Liang, X.L., Sun, F.T., Ming, Z., Liu, C., He, Y.P., and Lei, F.Z., 2019, Genesis of ore-bearing volcanic rocks in the Derbul lead–zinc mining area of the Erguna Massif, western slope of the Great Xing'an Range, NE China: Geochemistry, Sr–Nd–Pb isotopes, and zircon U–Pb geochronology: Geological Journal, v. 54, p. 3891–3908.

Yan, L.L., and Zhang, K.J., 2020, Infant intra-oceanic arc magmatism due to initial subduction induced by oceanic plateau accretion: A case study of the Bangong MesoTethys, central Tibet, western China: Gondwana Research, v. 79, p. 110–124.

Yin, A., and Harrison, T.M., 2000, Geologic evolution of the Himalayan–Tibetan orogeny: Annual Review of Earth and Planetary Sciences, v. 28, p. 211–280.

Yu, Y.P., Hu, P.Y., Li, C., Xie, C.M., Fan, J.J., Xu, W., and Liu, J.H., 2015, The Petrology and geochemistry of Early Cretaceous ocean island volcanic rocks in the middle-western segment of Bangong Co-Nujiang suture zone: Geological Bulletin of China, v. 35, p. 1281–1290 (in Chinese with English abstract).

Zeng, Y.C., Chen, J.L., Xu, J.F., Wang, B.D., and Huang, F., 2016, Sediment melting during subduction initiation: Geochronological and geochemical evidence from the Darutso high-Mg andesites within ophiolite melange, central Tibet: Geochemistry, Geophysics, Geosystems, v. 17, p. 4859-4877.

Zhai, Q. G., Jahn, B.M., Su, L., Ernst, R.E., Wang, K.L., Zhang, R.Y., Wang, J., and Tang, S.H., 2013, SHRIMP zircon U–Pb geochronology, geochemistry and Sr–Nd–Hf isotopic compositions of a mafic dyke swarm in the Qiangtang terrane, northern Tibet and geodynamic implications: Lithos, v. 174, p. 28–43.

Zhai, Q.G., Jahn, B.M., Wang, J., Hu, P.Y., Chung, S.L., Lee, H.Y., Tang, S.H., and Tang, Y., 2016. Oldest Paleo-Tethyan ophiolitic melange in the Tibetan Plateau: Geological Society of America Bulletin, v. 128, p. 355–373.

Zhang, K.J., Xia, B., Zhang, Y.X., Liu, W.L., Zeng, L., Li, J.F., and Xu, L.F., 2014a. Central Tibetan Meso-Tethyan oceanic plateau Lithos, v. 210–211, p. 278–288.

Zhang, X., Shi, R., Huang, Q., Liu, D., Gong, X., Chen, S., Wu, K., Yi, G., Sun, Y., and Ding, L., 2014b, Early Jurassic high-pressure metamorphism of the Amdo terrane, Tibet: Constraints from zircon U–Pb geochronology of mafic granulites: Gondwana Research, v. 26, p. 975–985.

Zhang, X.Z., Wang, Q., Dong, Y.S., Zhang, C., Li, Q.Y., Xia, X.P., and Xu, W., 2017, High pressure granulite-facies overprinting during the exhumation of eclogites in the Bangong-Nujiang suture zone, central Tibet: link to flat-slab subduction: Tectonics, v. 36, p. 2918–2935.

Zhang, Y.C., Shi, G.R., and Shen, S.Z., 2013, A review of Permian stratigraphy, palaeobiogeography and palaeogeography of the Qinghai–Tibet Plateau: Gondwana Research, v. 24, p. 55–76.

Zhang, Y.X., Li, Z.M., Zhu, L.D., Zhan, K.J., Yang, W.G., Jin, X., 2016, Newly discovered eclogites from the Bangong Meso–Tethyan suture zone (Gaize, central Tibet, western China): mineralogy, geochemistry, geochronology, and tectonic implications: International Geology Review, v. 58, p. 574–587.

Zhao, J.H., Zhou, M.F., 2007, Geochemistry of Neoproterozoic mafic intrusions in the Panzhihua district (Sichuan Province, SW China): Implications for subduction–related metasomatism in the upper mantle: Precambrian Research, v. 152, p. 27–47.

Zhong, Y., Liu, W.L., Xia, B., Liu, J.N., Guan, Y., Yin, Z.X., and Huang, Q.T., 2017, Geochemistry and geochronology of the Mesozoic Lanong ophiolitic mélange, northern Tibet: Implications for petrogenesis and tectonic evolution: Lithos, v. 292–293, p. 111–131.

Zhu, D.C., Pan, G.T., Mo, X.X., Wang, L.Q., Zhao, Z.D., Liao, Z.L., Geng, Q.R., and Dong, G.C., 2006, Identification for the Mesozoic OIB-type basalts in central Qinghai–Tibetan Plateau: geochronology, geochemistry and their tectonic setting: Acta Geological Sinica, v. 80, p. 1312–1328 (in Chinese with English abstract).

Zhu, D.C., Zhao, Z.D., Niu, Y., Dilek, Y., Hou, Z.Q., and Mo, X.X., 2013, The origin and pre-Cenozoic evolution of the Tibetan Plateau: Gondwana Research, v. 23, p. 1429–1454.

Zhu, D.C., Li, S.M., Cawood, P.A., Wang, Q., Zhao, Z.D., Liu, S.A., and Wang, L.Q., 2016, Assembly of the Lhasa and Qiangtang terranes in central Tibet by divergent double subduction: Lithos, v. 245, p. 7–17.

Zhu, Z., Zhai, Q., Hu, P., Chung, S., Tang, Y., Wang, H., Wu, H., Wang, W., Huang, Z., and Lee, H., 2019, Closure of the Bangong–Nujiang Tethyan Ocean in the central Tibet: Results from the provenance of the Duoni Formation: Journal of Sedimentary Research, v. 89, p. 1039–1054.

Figure Captions

Figure 1 (a) Tectonic framework of the Tibetan Plateau. EKASZ, East Kunlun–A'nyemaqen Suture Zone; JSSZ, Jinshajiang Suture Zone; LSLSZ, Longmuco–Shuanghu–Lancangjiang Suture Zone; BNSZ, Bangong–Nujiang Suture Zone; IYZSZ, Indus–Yarlung Zangbo Suture Zone. (b) Geological map of the middle and western segments of the BNSZ, showing the igneous and sedimentary rocks in the Zhonggang and Tarenben areas. (c) Field photograph of Zhonggang igneous–sedimentary rocks of the BNSZ.

Figure 2 (a) Geological map of the Zhonggang area. Cz, Cenozoic; K_1q, Lower Cretaceous Qushenla Formation comprising volcanic (108–103 Ma; Hao et al., 2019) and non-marine clastic rocks; J_3K_1s, Upper Jurassic–Lower Cretaceous Shamuluo Formation comprising marine sandstone, conglomerate, and limestone; J_{1-2}, Lower–Middle Jurassic Sewa, Shaqiaomu, and Jiebuqu formations dominated by marine sandstone and limestone; JM, Mugagangri Group comprising flysch deposits; DO, Dongco ophiolites that represent the remnants of a 180–162 Ma intra-oceanic arc (Fan et al., 2019; Li et al., 2019b); DG, 160–155 Ma Dongco granodiorite emplaced in the Dongco intra-oceanic arc sequence (Fan et al., 2016); OI, remnants of Middle Triassic–Jurassic intra-plate ocean island; ZISR, Zhonggang igneous–sedimentary rocks. (b) Remote sensing image from Google Earth showing the Zhonggang igneous–sedimentary rocks. (c) A typical two-layered structure comprising a thick basaltic basement and a limestone cover sequence. (d) Limestones interbedded with basalts within the cover sequence (Fan et al., 2014).

Figure 3 (a) Limestone interbedded with amygdaloidal basalt. (b) Basalt–tuff–limestone sequence. (c) Limestone interbedded with tuff. (d) Basalt–trachyandesite–limestone sequence. (e) Trachyandesite–limestone sequence. (f) Chert. (g) Reef limestone gravel within the colluvial conglomerate. (h, i) Typical exotic blocks-in-matrix structure between the Zhonggang igneous–sedimentary rocks and the surrounding flysch deposits.

Figure 4 Photomicrographs of the Zhonggang igneous–sedimentary rocks in cross-polarized light. (a) Basalt with carbonate alteration in the cover sequence. (b) Trachyandesite. (c) Limestone. (d) Limestone–tuff sequence. (e) Chert. (f) Colluvial conglomerate. Pl, plagioclase; Cal, calcite; B, basalt debris; Ls, limestone debris.

Figure 5 Immobile incompatible element discrimination diagram showing trachyandesite and basalt data.

Figure 6 (a) Chondrite-normalized REE variation diagram for the basalt. (b)

Primitive-mantle-normalized trace element variation diagram for the basalt. (c) Chondrite-normalized REE variation diagram for the trachyandesite. (d) Primitive-mantle-normalized trace element variation diagram for the trachyandesite. Normalizing values are from Sun and McDonough, 1989. OIB, ocean island basalt; BCC, bulk continental crust.

Figure 7 Representative cathodoluminescence images of zircon grains and zircon U–Pb concordia plots.

Figure 8 Diagram of $\varepsilon_{Nd}(t)$ vs. initial $^{87}Sr/^{86}Sr$ showing the basalt and trachyandesite samples, where (t) refers to the eruption ages (modified after Meng et al., 2015; Zhong et al., 2017). OIB, ocean island basalt; MORB, mid-ocean ridge basalt; DMM, depleted MORB mantle; EM, enriched mantle; LCC, lower continental crust; GLOSS, global subducting sediment.

Figure 9 (a) $\varepsilon_{Nd}(t)$ vs. SiO_2, (b) Sm/Yb vs. La/Sm (Aldanmaz et al., 2000). gt, garnet; sp, spinel. DM, depleted mantle; N-MORB, normal-mid-ocean-ridge basalt; PM, primitive mantle.

Figure 10 Schematic illustrations of typical intra-plate ocean island lithostratigraphic sequences for (a) Hawaii-type ocean island. (b) Cape Verde-type ocean island.

Figure 11 Initial Sr–Nd isotope plot for the trachyandesite and basalt (modified after Widom et al., 1997; Elliott et al., 2007; Tanaka et al., 2008; Garapić et al., 2015; Mata et al., 2017).

Figure 12 Schematic illustration of the Zhonggang igneous–sedimentary rocks: (a) During development of the ocean island; (b) After the Lhasa–Qiangtang collision.

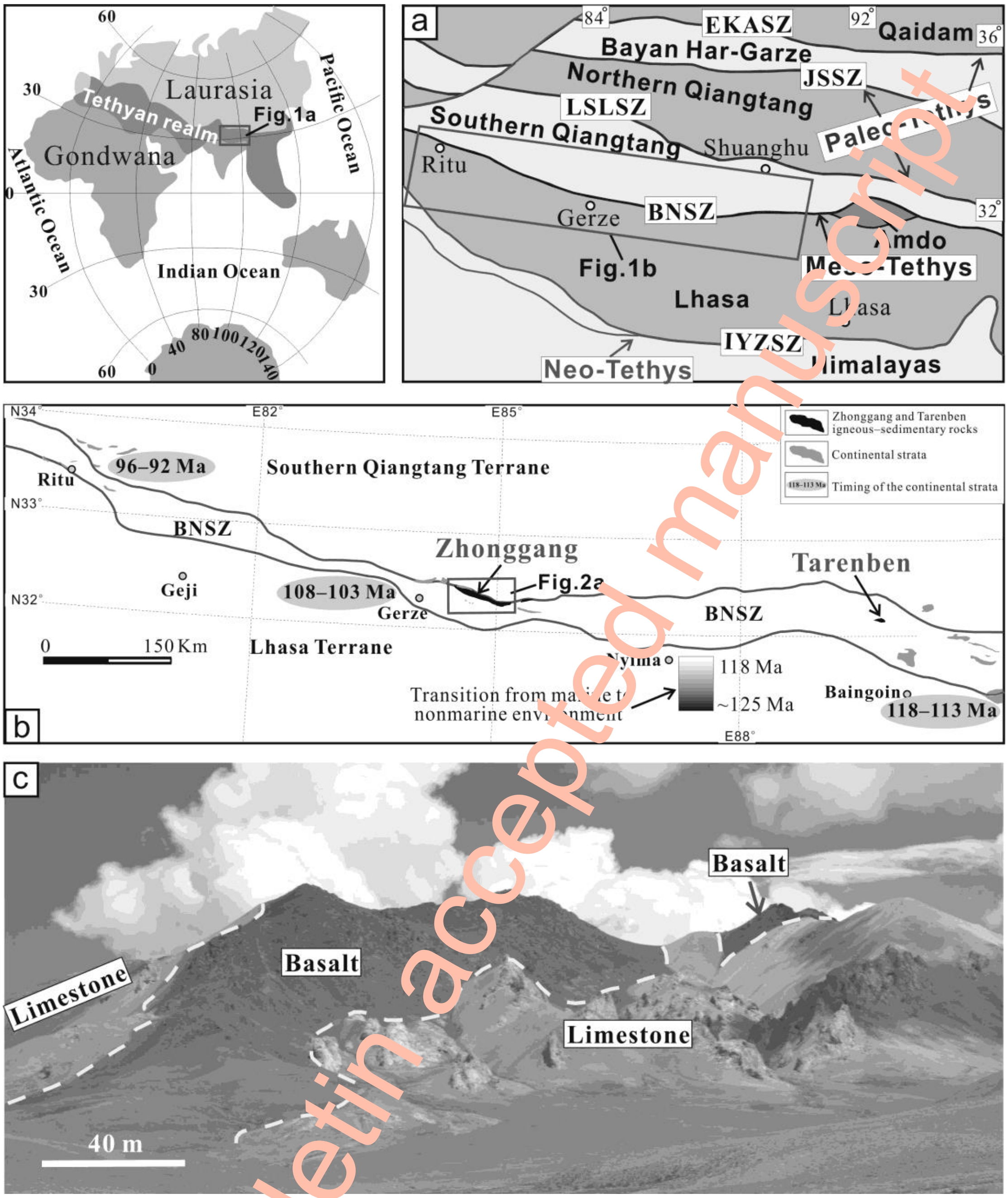

Laurasia
Tethyan realm
Fig.1a
Gondwana
Pacific Ocean
Atlantic Ocean
Indian Ocean
a
EKASZ
Bayan Har-Garze
Qaidam
Northern Qiangtang
JSSZ
LSLSZ
Southern Qiangtang
Shuanghu
Ritu
Gerze
BNSZ
Fig.1b
Lhasa
IYZSZ
Neo-Tethys
b
96–92 Ma
Southern Qiangtang Terrane
Ritu
BNSZ
Zhonggang
Fig.2a
Tarenben
Geji
108–103 Ma
Gerze
150 Km
Lhasa Terrane
118 Ma
~125 Ma
Baingoin
118–113 Ma
Zhonggang and Tarenben igneous–sedimentary rocks
Continental strata
Timing of the continental strata
c
Basalt
Limestone
Basalt
Limestone
40 m

Fig. 1

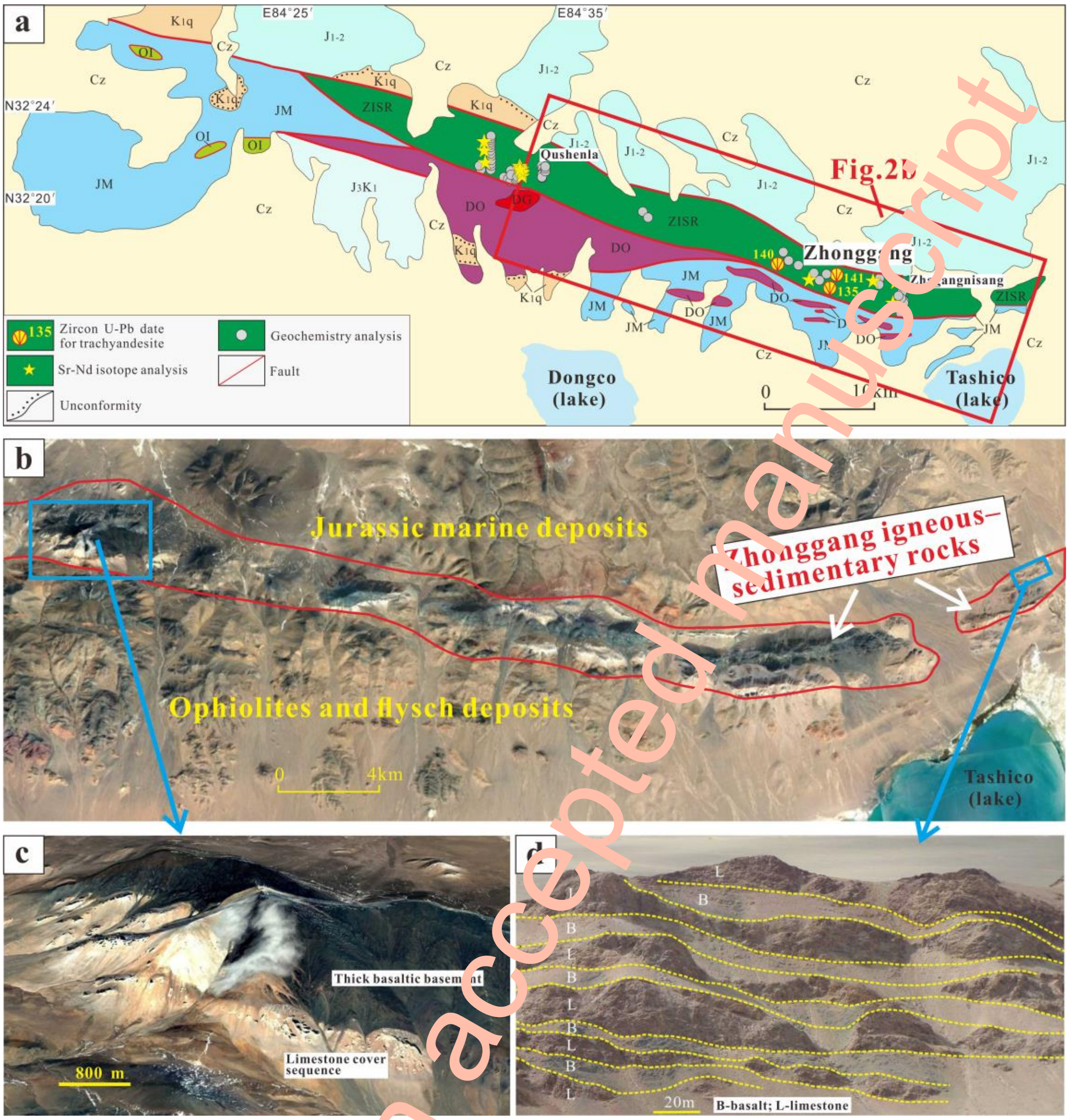
a
b
c
d
Jurassic marine deposits
Zhonggang igneous–sedimentary rocks
Ophiolites and flysch deposits
Tashico (lake)
Dongco (lake)
Qushenla
Zhonggang
Zhongangnisang
Fig.2b
Zircon U-Pb date for trachyandesite
Sr-Nd isotope analysis
Unconformity
Geochemistry analysis
Fault
Thick basaltic basement
Limestone cover sequence
800 m
20m
B-basalt; L-limestone
4km

Fig. 2

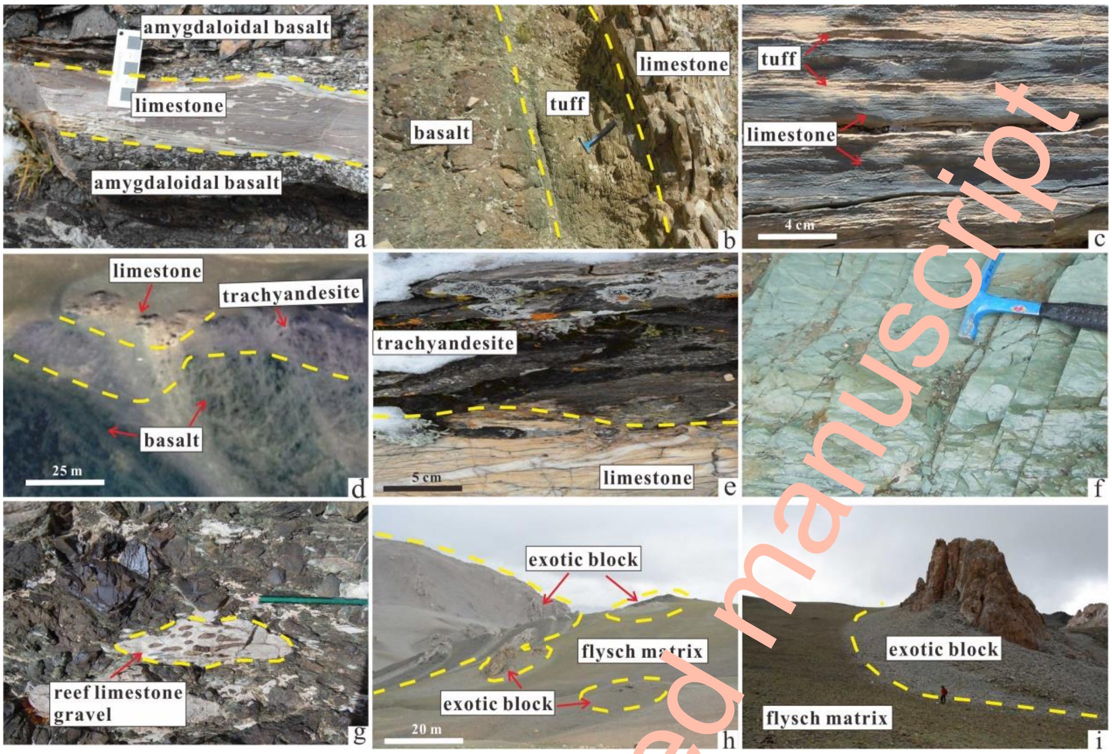
amygdaloidal basalt
limestone
amygdaloidal basalt
a
limestone
tuff
basalt
b
tuff
limestone
4 cm
c
limestone
trachyandesite
basalt
25 m
d
trachyandesite
5 cm
limestone
e
f
reef limestone
gravel
g
exotic block
flysch matrix
exotic block
20 m
h
exotic block
flysch matrix
i

Fig. 3

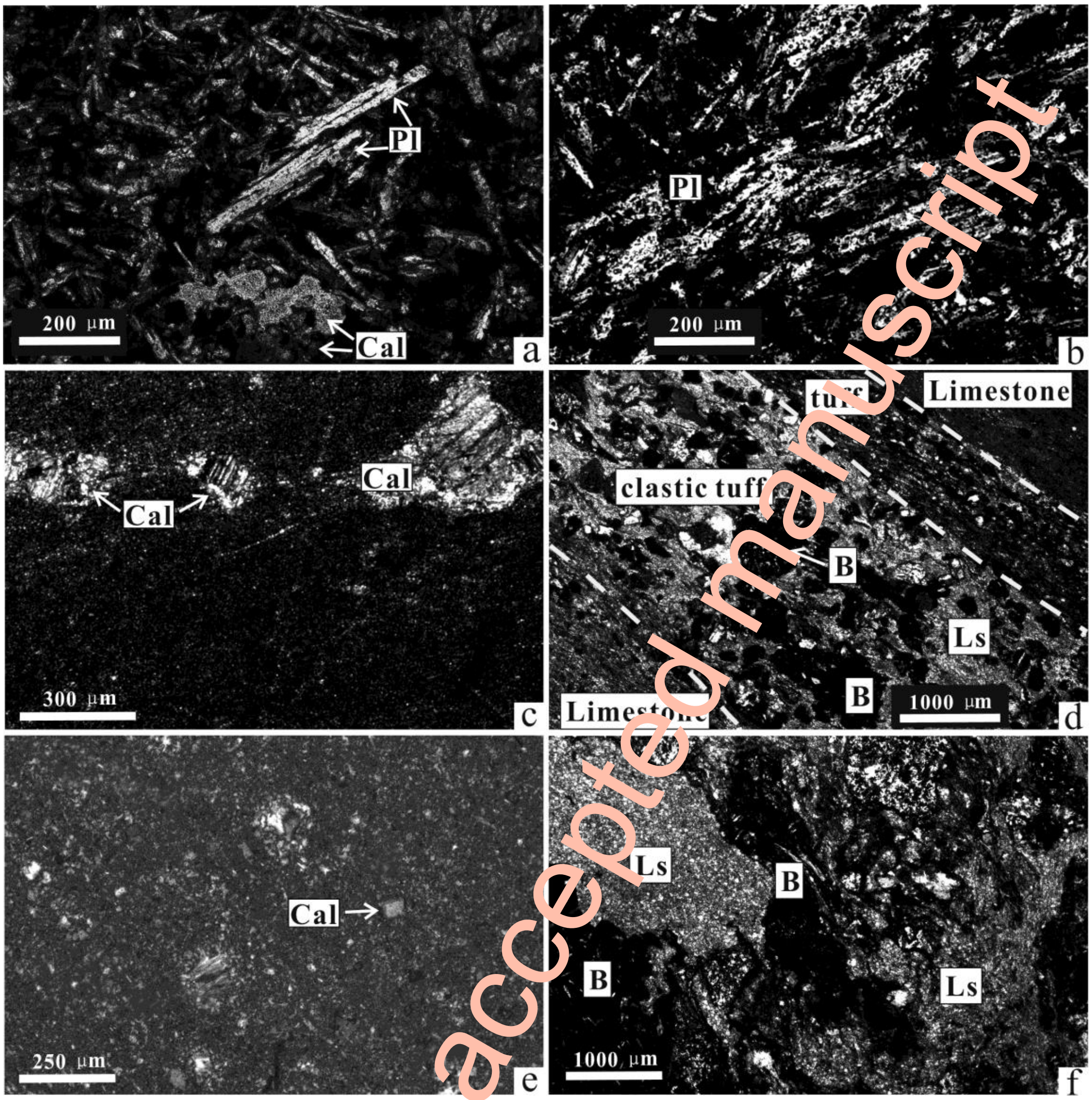

Pl
Pl
200 µm
Cal
a
Pl
200 µm
b
Cal
Cal
300 µm
c
Limestone
clastic tuff
B
Ls
B
1000 µm
d
Cal
250 µm
e
Ls
B
B
Ls
1000 µm
f

Fig. 4

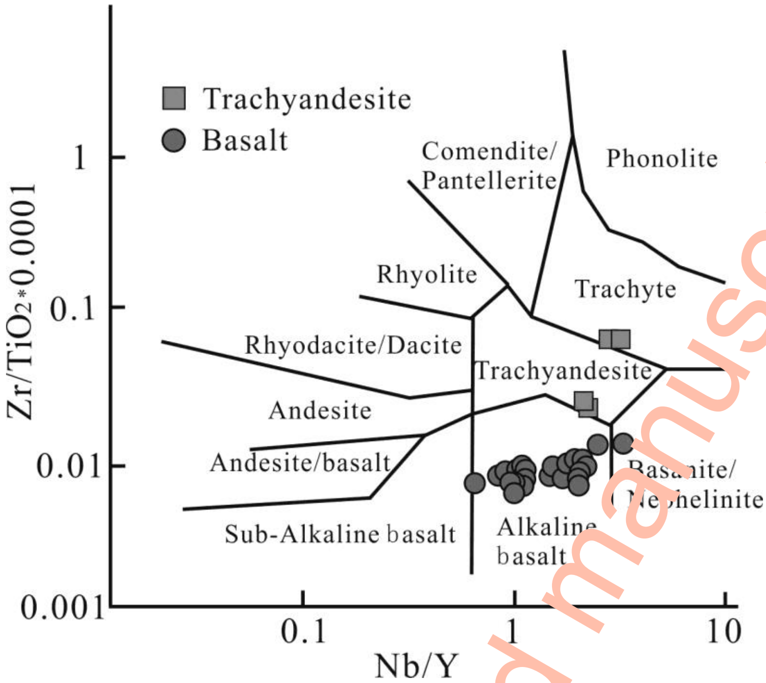

Trachyandesite
Basalt
Zr/TiO2*0.0001
Nb/Y
Comendite/
Pantellerite
Phonolite
Rhyolite
Trachyte
Rhyodacite/Dacite
Trachyandesite
Andesite
Andesite/basalt
Sub-Alkaline basalt
Alkaline
basalt

Fig. 5

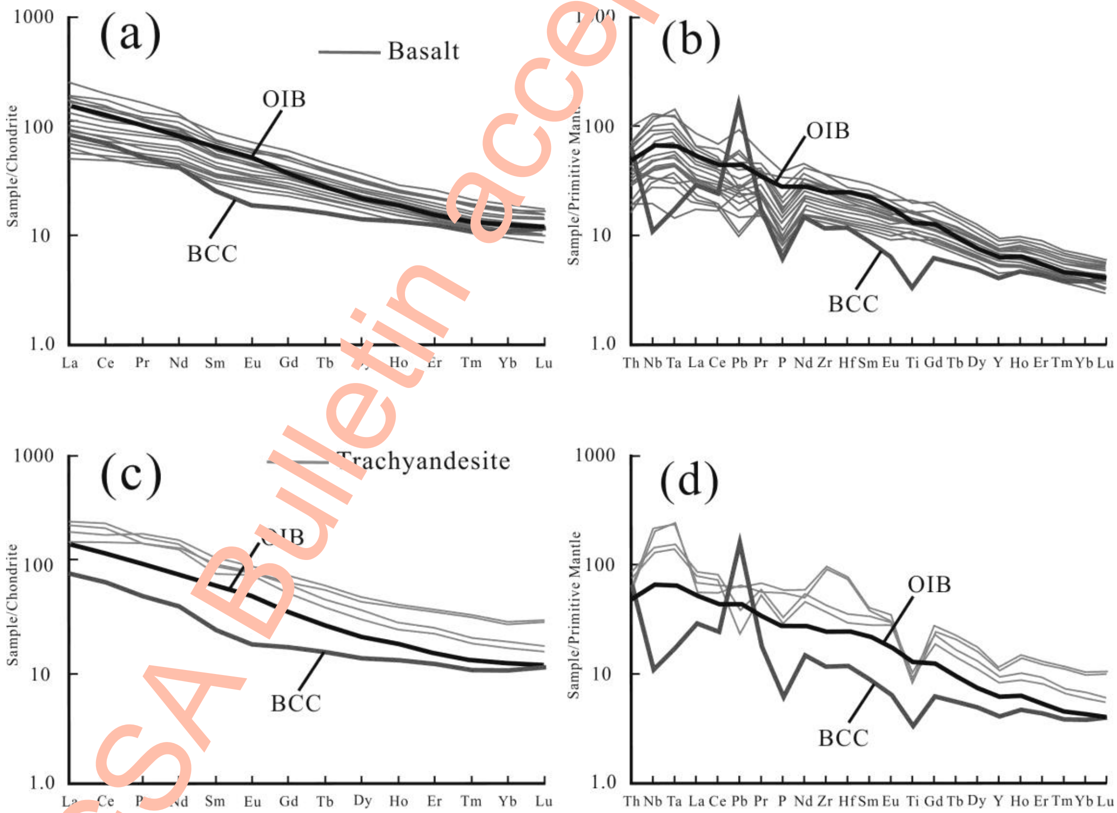

(a)
Basalt
OIB
BCC
Sample/Chondrite
La Ce Pr Nd Sm Eu Gd Tb Dy Ho Er Tm Yb Lu
(b)
OIB
BCC
Sample/Primitive Mantle
Th Nb Ta La Ce Pb Pr P Nd Zr Hf Sm Eu Ti Gd Tb Dy Y Ho Er Tm Yb Lu
(c)
Trachyandesite
OIB
BCC
(d)
OIB
BCC

Fig. 6

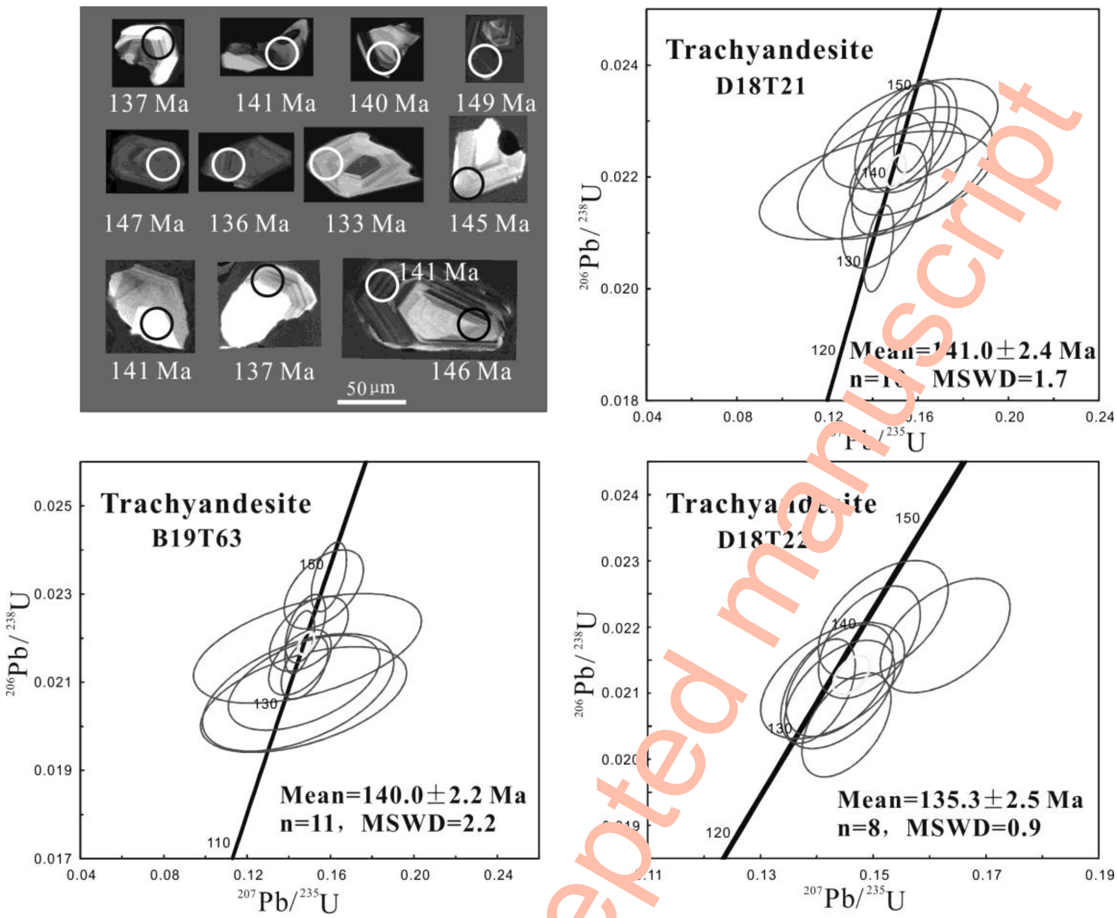

137 Ma
141 Ma
140 Ma
149 Ma
147 Ma
136 Ma
133 Ma
145 Ma
141 Ma
141 Ma
137 Ma
146 Ma
50 μm
Trachyandesite
D18T21
Mean=141.0±2.4 Ma
MSWD=1.7
Trachyandesite
B19T63
Mean=140.0±2.2 Ma
n=11, MSWD=2.2
$^{206}Pb/^{238}U$
$^{207}Pb/^{235}U$
Mean=135.3±2.5 Ma
n=8, MSWD=0.9

Fig. 7

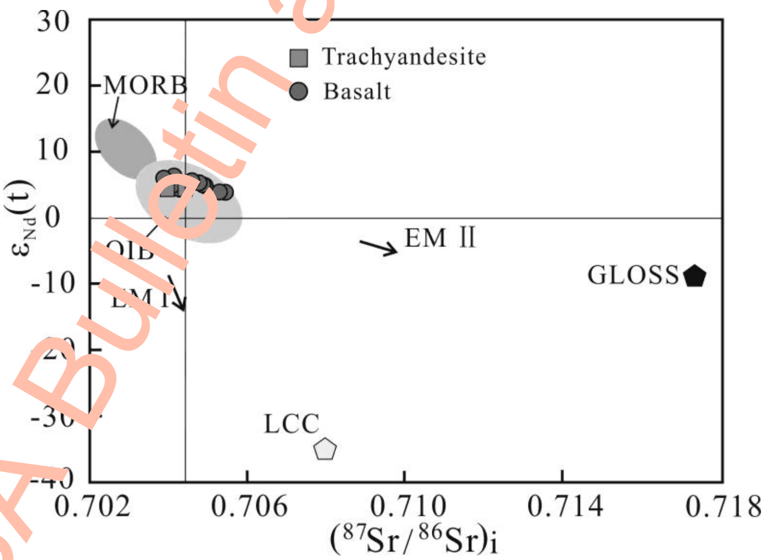

Trachyandesite
Basalt
MORB
OIB
EM Ⅱ
EM Ⅰ
GLOSS
LCC
$\varepsilon_{Nd}(t)$
$(^{87}Sr/^{86}Sr)_i$

Fig. 8

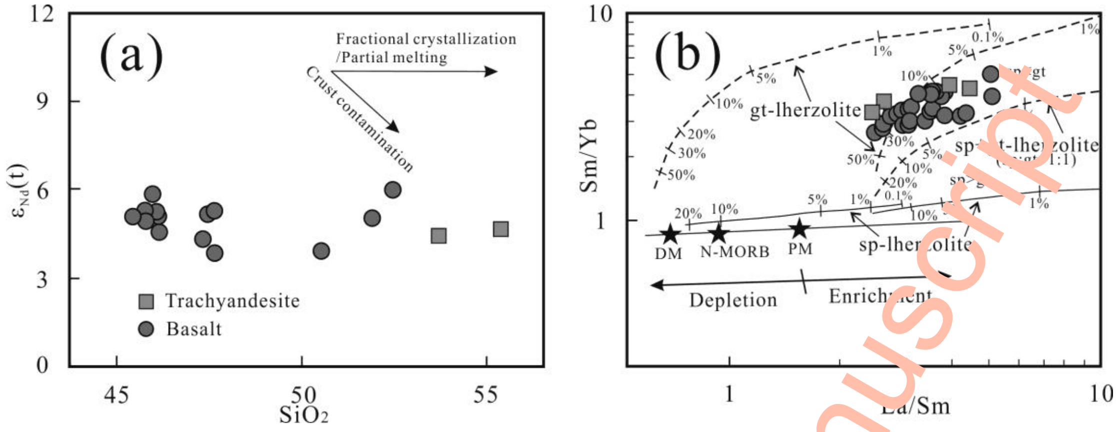

(a)
Fractional crystallization
/Partial melting
Crust contamination
Trachyandesite
Basalt
εNd(t)
SiO2
(b)
gt-lherzolite
sp-lherzolite
DM
N-MORB
PM
Depletion
Enrichment
Sm/Yb
La/Sm

Fig. 9

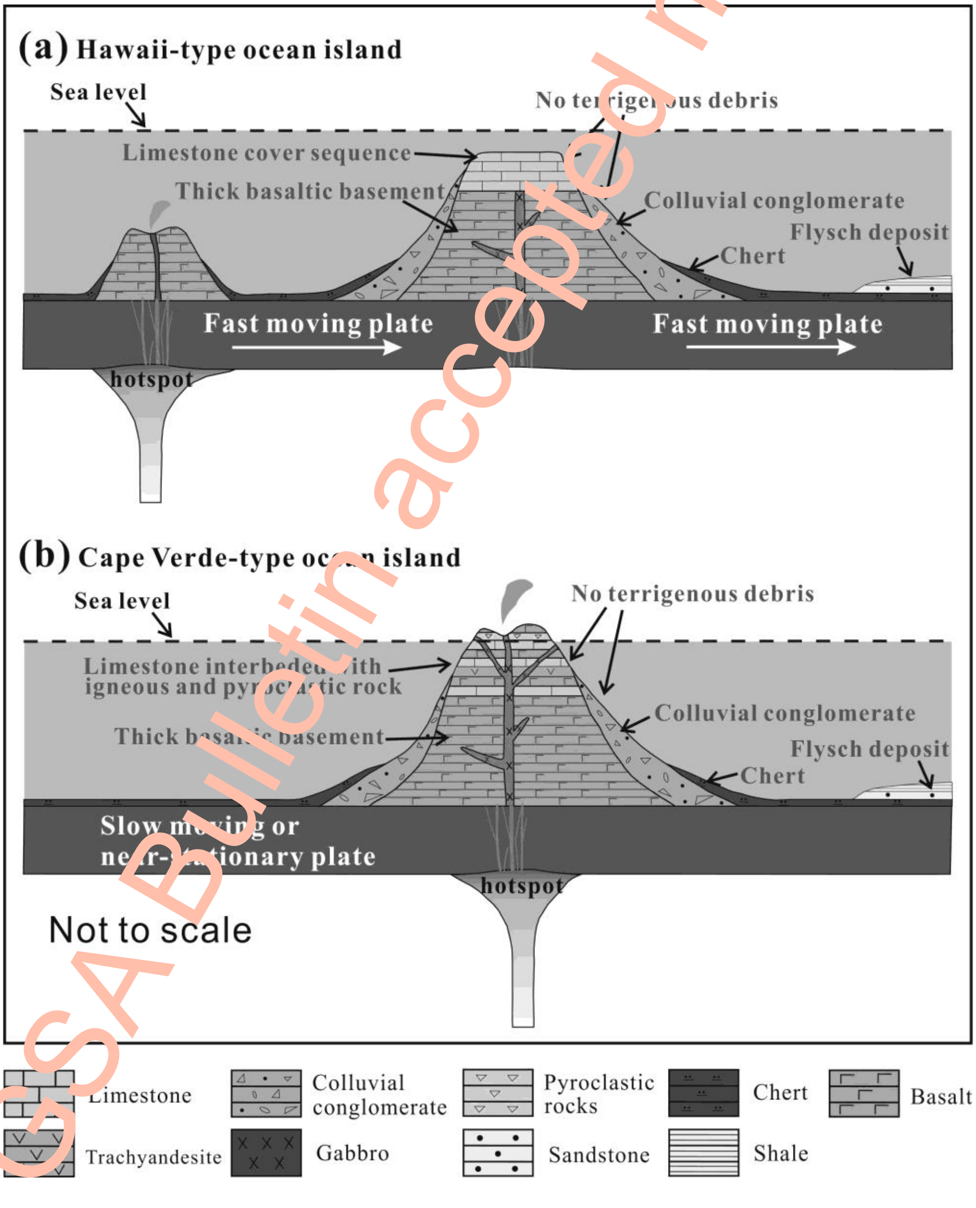

(a) Hawaii-type ocean island
Sea level
No terrigenous debris
Limestone cover sequence
Thick basaltic basement
Colluvial conglomerate
Flysch deposit
Chert
Fast moving plate
Fast moving plate
hotspot
(b) Cape Verde-type ocean island
Sea level
No terrigenous debris
Limestone interbedded with
igneous and pyroclastic rock
Thick basaltic basement
Colluvial conglomerate
Flysch deposit
Chert
Slow moving or
near-stationary plate
hotspot
Not to scale
Limestone
Colluvial conglomerate
Pyroclastic rocks
Chert
Basalt
Trachyandesite
Gabbro
Sandstone
Shale

Fig. 10

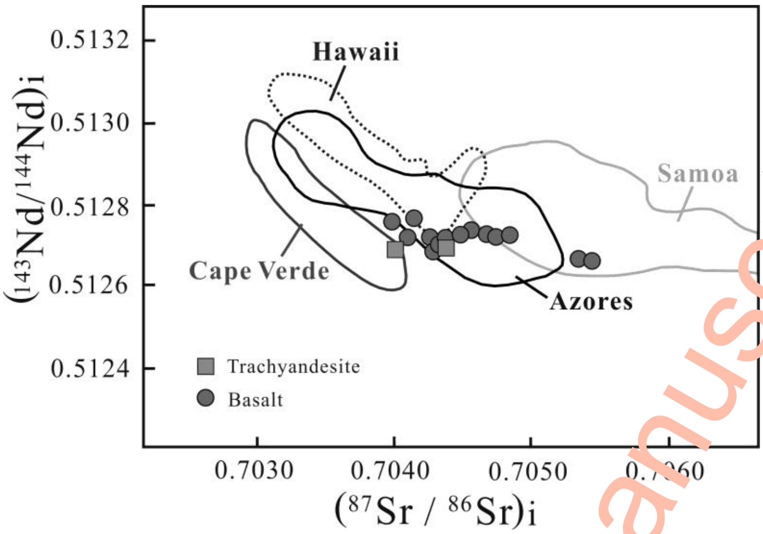

Hawaii
Samoa
Cape Verde
Azores
Trachyandesite
Basalt
0.5132
0.5130
0.5128
0.5126
0.5124
0.7030
0.7040
0.7050
0.7060
$(^{143}Nd/^{144}Nd)_i$
$(^{87}Sr/^{86}Sr)_i$

Fig. 11

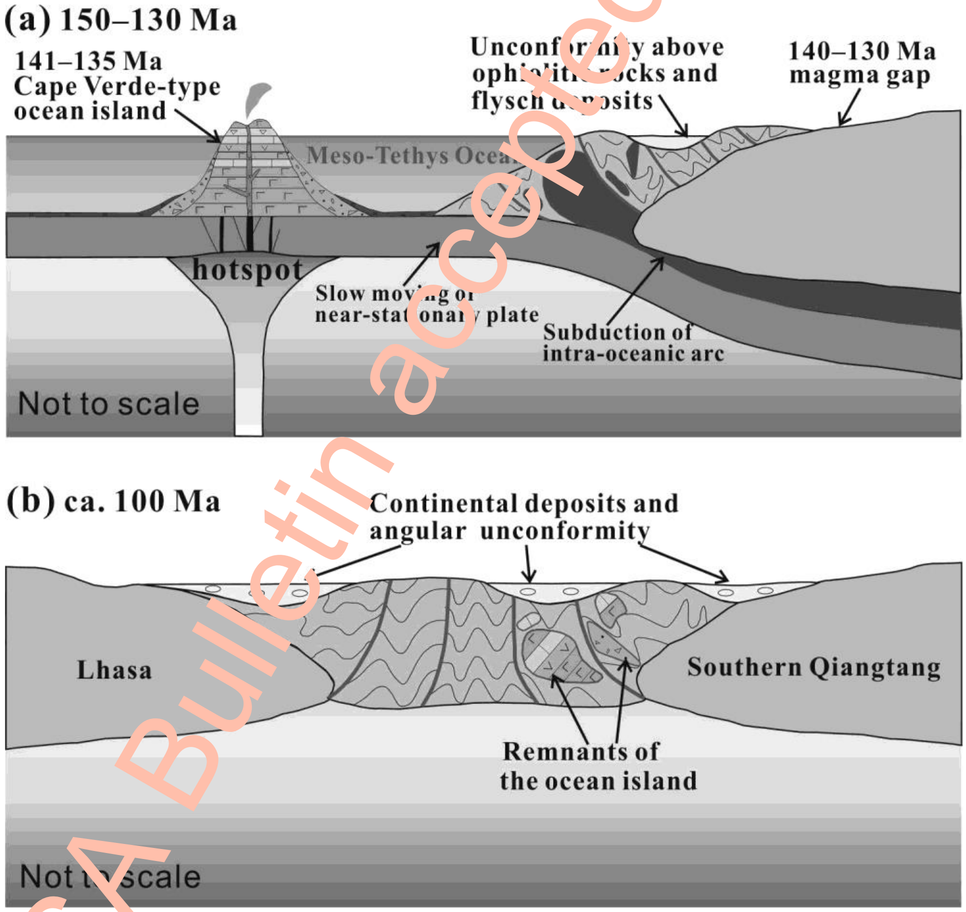

(a) 150–130 Ma
141–135 Ma
Cape Verde-type
ocean island
Unconformity above
ophiolitic rocks and
flysch deposits
140–130 Ma
magma gap
Meso-Tethys Ocean
hotspot
Slow moving or
near-stationary plate
Subduction of
intra-oceanic arc
Not to scale
(b) ca. 100 Ma
Continental deposits and
angular unconformity
Lhasa
Southern Qiangtang
Remnants of
the ocean island
Not to scale

Fig. 12